

# Potential formation mechanisms of early diagenetic displacive veins in the Permian Boda Claystone Formation

Ervin Hrabovszki<sup>a,\*</sup>, Emese Tóth<sup>a</sup>, Tivadar M. Tóth<sup>a</sup>, Zoltán Máthé<sup>b</sup>, Félix Schubert<sup>a</sup>

<sup>a</sup> Department of Mineralogy, Geochemistry and Petrology, University of Szeged, 6722, Szeged, Hungary

<sup>b</sup> Mecsekérc Ltd., 7633, Pécs, Hungary

## ARTICLE INFO

### Keywords:

Solid inclusions  
Cone-in-cone structures  
Continuous vein growth  
Force of crystallisation  
Seepage forces  
Bedding-parallel veins

## ABSTRACT

The Boda Claystone Formation is the most promising host rock for the disposal of high-level radioactive waste in Hungary. The formation has several properties obstructing the migration of radionuclides; however, structural heterogeneities may nonetheless act as migration pathways. Therefore, understanding the tectonic evolution of the formation is vital. Previous research has identified four different vein generations in the BAF-2 well. This study deals with the generation of veins that contain characteristic microstructures, such as curved wall rock inclusions in bands, trails and cone-in-cone arrangements. Based on optical, cathodoluminescence and electron microscopy, together with X-ray fluorescence and Raman microspectroscopy, these veins appear to have potentially formed during early diagenetic processes. Vein development was continuous and occurred along horizontal surfaces. The abovementioned structural elements were formed by growing crystals; however, primary crystal morphologies were presumably replaced during diagenetic and hydrothermal processes. A theoretical model is described, which could be responsible for the horizontal and continuous vein opening and simultaneous crystallisation in sediments with high (but easily degraded) effective porosity. According to this model, compaction, pressure solution, elevated pore fluid pressures, seepage forces and the force of crystallisation can all play important roles in the formation of these types of veins.

## 1. Introduction

National screening (Konrád and Hámos, 2006) of geological formations has revealed that the Late Permian Boda Claystone Formation (BCF) is a potential host rock for the deep geological repository of high-level radioactive waste in Hungary. The porosity and permeability of this 500–1000-m-thick claystone are ideally low for hazardous waste isolation (Fedor et al., 2008). Nonetheless, rocks with such properties are often characterised by significant fluid flow along planes associated with their structural inhomogeneities. For this reason, it is crucial to understand how the phases of structural evolution and palaeo-fluid flow history of the BCF are recorded by fractures and veins within.

As reported by Hrabovszki et al. (2017), most veins throughout the BCF can be classified based on the classical scheme of vein growth morphologies (Ramsay and Huber, 1983; Bons, 2000; Passchier and Trouw, 2005; Bons et al., 2012) into the following categories: 1) Syntaxial veins—the vein-forming elongate blocky crystals grew from the wall rock towards the vein centres. 2) Antitaxial veins—the crystal fibres grew from the median zones of the veins towards the vein sides. 3)

Ataxial veins—the stretched crystals showed no systematic growth direction. However, the subhedral, mosaic, acicular and fibrous crystal morphologies of a unique, polytextured vein generation is not consistent with its microstructure. These kinds of veins contain curved wall rock inclusions (WRI), which are frequently aligned in inclusion bands, inclusion trails and cone-in-cone (CIC; Cobbold and Rodrigues, 2007; Cobbold et al., 2013) arrangements.

In this paper, microstructural characteristics of WRI-containing veins were presented, such as extremely variable sized host rock fragments, partially detached solid inclusions and diffuse WRI boundaries. These observations suggest that the studied vein generation does not relate to tectonic processes but were formed because of compaction, pressure solution, elevated fluid pressure, vertical fluid migration and force of crystallisation during early diagenesis. The inclusion bands, trails and CIC structures were formed by growing fibrous crystals that were replaced during a later stage of the vein evolution. These findings indicate that understanding the formation of microstructures and microscopic morphologies of veins contribute to the reconstruction of structural evolution and paleofluid flow history of such environments.

\* Corresponding author.

E-mail address: [ervin.hrabovszki@geo.u-szeged.hu](mailto:ervin.hrabovszki@geo.u-szeged.hu) (E. Hrabovszki).

<https://doi.org/10.1016/j.jsg.2020.104098>

Received 15 January 2020; Received in revised form 27 May 2020; Accepted 28 May 2020

Available online 3 June 2020

0191-8141/© 2020 The Authors. Published by Elsevier Ltd. This is an open access article under the CC BY license (<http://creativecommons.org/licenses/by/4.0/>).

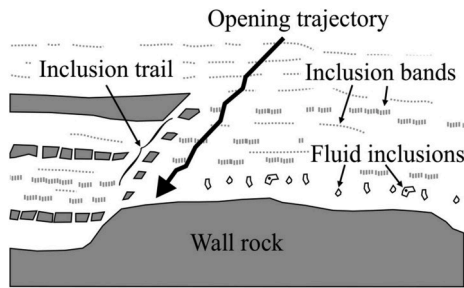


**Fig. 1.** Solid (and fluid) inclusion arrangements within veins based on the work of Passchier and Trouw (2005). Inclusion trails are usually parallel to the vein opening trajectory, whereas inclusion bands dominantly reflect the orientation of the vein walls.

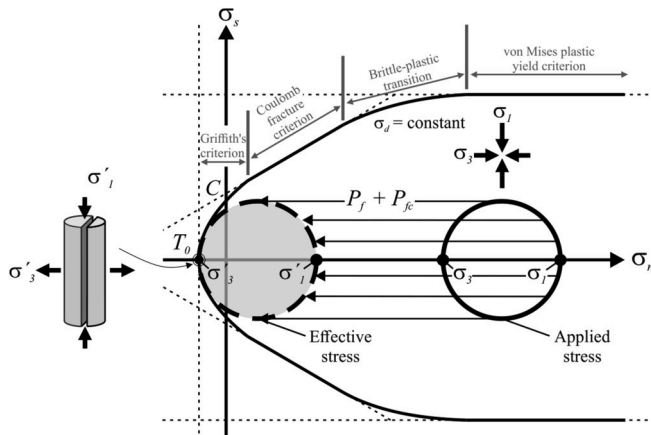


**Fig. 2.** The effect of increasing fluid pressure ( $P_f$ ) and crystallisation pressure ( $P_{fc}$ ) on the stress field and fracture formation. The Mohr circle of constant size shifts left along the  $\sigma_n$  axis by the amount of  $P_f$  and  $P_{fc}$ . If the Mohr circle for effective stress touches the failure envelope in the tensile field of the Mohr space at one point on the  $\sigma_n$  axis, tensile fracture occurs. If no tectonic stress is present, the greatest ( $\sigma'_1$ ) and least ( $\sigma'_3$ ) effective stresses are vertical and horizontal owing to the lithostatic pressure; therefore, the fracture will be vertical.

### 1.1. Formation mechanisms of inclusion bands and inclusion trails

Generally, two distinct types of inclusion arrangements in veins are distinguished in the literature (e.g. Ramsay, 1980): inclusion bands and inclusion trails. *Inclusion bands* are surfaces of solid (and fluid) inclusions reflecting the orientation and shape of the vein-wall interface (Fig. 1, Passchier and Trouw, 2005). Each band represents a single episode of the vein opening history; therefore, the distance between two bands is equal to the width of a single opening and sealing increment. *Inclusion trails* are also aggregates of solid (and fluid) inclusions; however, they occur along surfaces sub-perpendicular to the walls of the vein (Fig. 1, Passchier and Trouw, 2005). These surfaces usually connect corresponding points between adjacent inclusion bands and therefore the vein walls; as a result, they record the opening trajectory of veins (Ramsay and Huber, 1983; Cox, 1987; Koehn and Passchier, 2000; Passchier and Trouw, 2005; Renard et al., 2005). There are two preferred mechanisms for the formation of both microstructures: a) the crack-seal mechanism and b) continuous opening and cementation.

The crack-seal process involves periodic opening and sealing events in a narrow cavity (Ramsay, 1980) due to hydraulic fracturing (Hubbert and Willis, 1957). In the case of elevated pore fluid pressure ( $P_f$ ), the rock behaves as if the applied stress were lower by the amount  $P_f$ ; the result being termed *effective stress* ( $\sigma'$ ; Twiss and Moores, 1992). In other words, a Mohr circle of equivalent size shifts along the normal stress axis

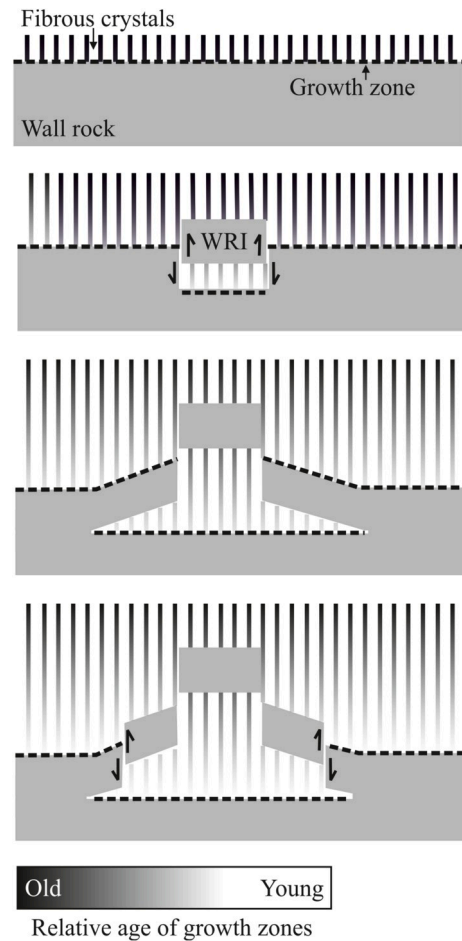


**Fig. 3.** The constant growth rate model of fibrous veins and the formation of sinusoidal inclusions based on the work of Hilgers and Urai (2005). According to this model, fibrous crystals grow at a constant rate along the vein-wall interface. As vein growth progresses, crystals precipitate with similar crystallographic orientations in the host rock. This might be possible only if the crystals precipitate before the separation of the wall rock inclusion (WRI). During the process, there is no shear between adjacent fibrous crystals, only between the wall rock and the detaching WRIs.

towards smaller compressive stresses. If  $P_f$  exceeds the minimum compressive stress ( $\sigma_3$ ) by an amount equal to the tensile strength ( $T_0$ ) of the rock, fracturing can occur. Depending on the amount of differential stress extensional, mixed-mode (hybrid) or shear fractures can develop. Due to fracturing,  $P_f$  decreases, and decreasing the solubility of the materials dissolved in the fluids filling these micro-cracks leads to the sealing of cracks by minerals (Van der Pluijm and Marshak, 2004). In addition to pressure reduction, fluids may become supersaturated due to changes in temperature, pH, Eh, evaporation, pressure solution or fluid mixing (Bons et al., 2012). After the sealing of fluid pathways,  $P_f$  increases again until the rock fails. This cycle can be repeated hundreds of times. Each time a new crack forms at the vein-wall rock contact, solid fragments can break off and be incorporated by crystals during the sealing process.

Veins can also form by continuous opening and cementation without the presence of any open fractures (Means and Li, 2001; Wiltchko and Morse, 2001; Hilgers and Urai, 2005; Hilgers et al., 2006). Solid inclusion bands and trails can develop during continuous vein formation caused by the force of crystallisation (Taber, 1916; Means and Li, 2001). The pressure generated by crystal growth ( $P_{fc}$ ) acts similarly to vein formation in terms of the pore fluid pressure involved in hydrofracture development (Fig. 2; Wiltchko and Morse, 2001). The magnitude of  $P_{fc}$  is related to the level of supersaturation in the pore fluid (Dewers and

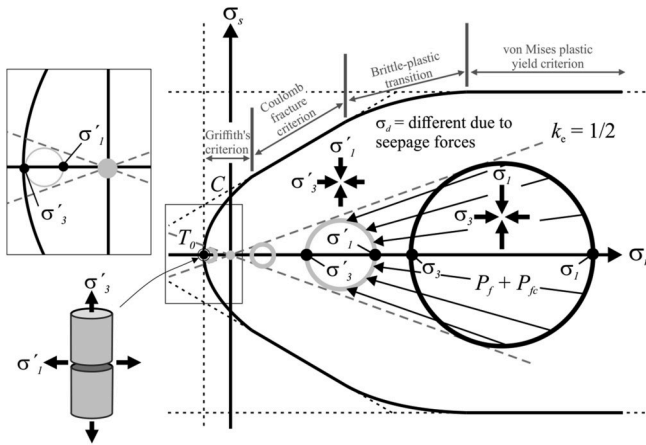


**Fig. 4.** The formation of horizontal fractures induced by fluid overpressure ( $P_f$ ) and crystallisation pressure ( $P_{fc}$ ) in the presence of seepage forces based on Cobbold and Rodrigues (2007). The Mohr circle for effective stress ( $\sigma'$ ) in the compressional field gradually shifts to the left and decreases in size as a result of growing  $P_f + P_{fc}$  and seepage forces. Further increase in  $P_f + P_{fc}$  results in an increased differential stress ( $\sigma_d$ ) in the tensional field of the Mohr space. As a result, the least effective stress ( $\sigma'_3$ ) becomes vertical.  $k_e$  is the elastic constant of proportionality.

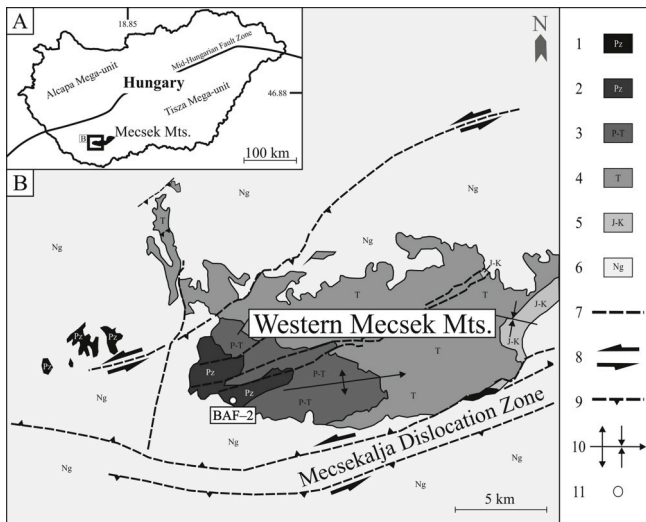


**Fig. 5.** A–Location of the Mecsek Mountains within Hungary. B–Distribution of the Boda Claystone Formation (modified after Konrád and Sebe, 2010). Legend: 1–all Palaeozoic; 2–Upper Permian Boda Claystone Fm; 3–Late Permian Kővágószőlő Sandstone Fm; 4–Triassic sediments (sandstones, carbonates, evaporites); 5–Jurassic and Cretaceous sediments and Cretaceous volcanic rocks; 6–Neogene sediments; 7–fault; 8–strike-slip fault; 9–thrust fault; 10–syncline and anticline; 11–well site.

Ortoleva, 1990; Wiltshko and Morse, 2001) given by Equation (1):

$$P_{fc} = \left( \frac{RT}{-\Delta V} \right) \ln \Omega, \quad (1)$$

where  $R$  is the gas constant,  $T$  is temperature,  $\Delta V$  is the change of volume between a substance in solution and its precipitate, and  $\Omega$  is the degree of supersaturation in the pore fluid. Therefore, an increase in supersaturation increases the pressure generated by crystallisation ( $P_{fc}$ ). By way of example, if the NaCl saturation level is  $\sim 1.5$ , pressures can reach 135 MPa (Desarnaud et al., 2016). In such cases, fluid advection is not required for vein growth, since diffusion can be a very effective mechanism for material transport even in stagnant pore fluids (Bons, 2000).

Fibrous crystals can grow at the vein-wall rock contacts until supersaturation of the pore fluid is sufficiently high (Wiltshko and Morse, 2001).

Based on the sinusoidal arrangement of solid inclusions within fibrous veins, Hilgers and Urai (2005) concluded that veins grew continuously according to their ‘constant growth rate’ model (Fig. 3). The inclusion arrangements described in their study formed at least partly due to the force of crystallisation and not by the classic crack-seal mechanism.

## 1.2. Cone-in-cone structures within bedding-parallel veins

CIC structures are common in bedding-parallel fibrous veins, known as beef (Cobbold et al., 2013 and references therein), of low-permeability sedimentary rocks. They typically appear as fibrous crystals and conical WRI series between them. Such veins develop as horizontal planes with vertical openings and crystal growth directions (Selles-Martinez, 1994; Rodrigues et al., 2009). The mineral cement of CIC-containing veins is dominantly calcite, gypsum (satin spar) or quartz; however, other minerals may also develop with fibrous morphology depending on the suppression (or absence) of competition between the growing crystals (Bons, 2000; Hilgers et al., 2001). CIC structures comprise concentric interbedded cones of fibrous crystals with thin layers of host rock material, which is commonly mudstone, evaporite or, in rarer cases, carbonate. Host rock inclusions usually form boundaries between adjacent cones (Kolokol'tsev, 2002). The CIC structure was first described in the 19th century (Sorby, 1860), but several crucial concepts towards understanding its formation mechanism have emerged only in the last decades, including aragonite–calcite transformation (Tarr, 1922), volume shrinkage during dewatering (Shaub, 1937), convective heat and mass transfer (Kolokol'tsev, 2002), seismic wave propagation (Ábalos and Elorza, 2011), displacive crystal growth (Taber, 1916; Woodland, 1964; Franks, 1969) and fluid overpressure-induced fracturing (Meng et al., 2017), among others. Nevertheless, most authors agree that the structure develops through the formation of fibrous crystals within partially consolidated sediments during early diagenesis.

Cobbold and Rodrigues (2007) provided a comprehensive explanation of how the greatest effective stress vector may become horizontal and thus how horizontal veins may develop in tectonically inactive sedimentary basins. The primary condition is that pore fluid migrates upward in response to a vertical gradient in fluid overpressure caused by mechanical compaction. Due to this migration, seepage forces act on the framework grains of the sediment. The vertical effective stress is reduced by the amount of fluid overpressure as shown in Equation (2) (modified after Cobbold and Rodrigues, 2007):

$$\sigma'_1 = \sigma_1 - P_f \quad (2)$$

Here,  $\sigma'_1$  is the greatest effective stress,  $\sigma_1$  is the greatest applied stress and  $P_f$  is fluid pressure. Since there is no horizontal fluid migration, the horizontal effective stress ( $\sigma'_3$ ) is not modified by seepage forces; instead, it is proportional to the vertical effective stress as shown in Equation (3) (modified after Cobbold and Rodrigues, 2007):

$$\sigma'_3 = k_e \sigma'_1 = k_e (\sigma_1 - P_f), \quad (3)$$

where  $k_e$  is an elastic constant of proportionality derived from Poisson's ratio ( $\nu$ ):

$$k_e = \left( \frac{\nu}{1 - \nu} \right) \quad (4)$$

Accordingly, in cases of increasing overpressure, the Mohr circle decreases in size and shifts along the normal stress axis to the left. For the formation of bedding-parallel veins, the Mohr circle is required to touch the failure envelope in the tensile stress field. This is achievable when  $P_f$  exceeds the pressure resulting from the weight of the

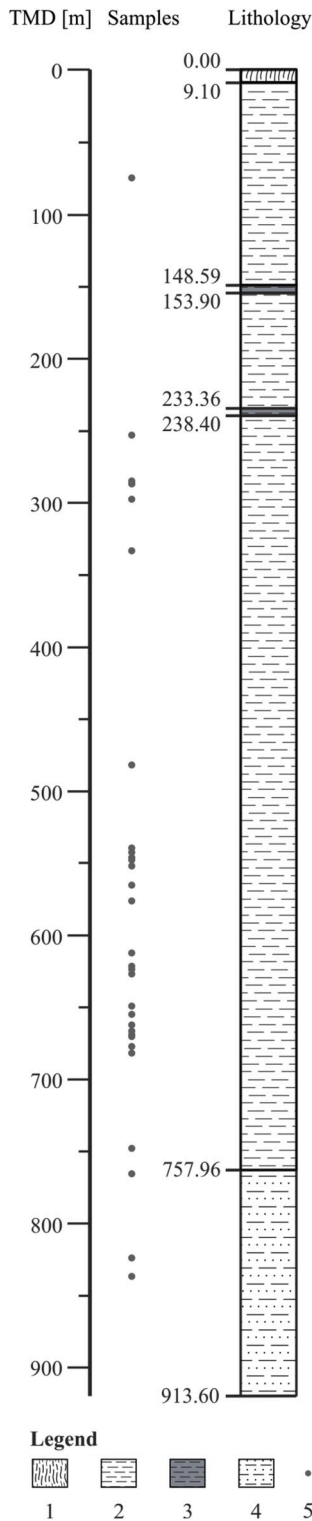


**Fig. 6.** The stratigraphical column of the BAF-2 well with the total measured depth (TMD) of the collected drill core samples (based on Konrád et al., 2016). Legend: 1–soil, loess; 2–claystone with siltstone interbeds; 3–greenish-black reductive claystone; 4–claystone with siltstone and sandstone interbeds; 5–location of drill core samples investigated in this study.

overburden. In such cases, the former  $\sigma'_1$  becomes larger in the tensile field and changes into the least effective stress ( $\sigma'_3$ ), which acts vertically. Under these conditions ( $P_f > \sigma_3$ ), the horizontal effective stress is:

$$\sigma'_1 = k_c \sigma'_3 = k_c (\sigma_1 - P_f), \quad (5)$$

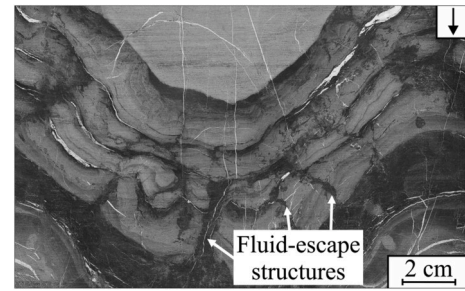


**Fig. 7.** Fluid-escape structures in a stitched core scanner image of the drill core sample from the depth interval of 548.40–548.66 m (TMD). Note that sinuoidal bedding surfaces are artefacts instead of folds and represent inclined bedding on the cylinder wall. The arrow in the upper right corner indicates the axis of the core sample and the down direction.

where  $\sigma'_1$  is the horizontal effective stress,  $\sigma'_3$  is the vertical effective stress and  $\sigma_1$  is the greatest applied stress. Thus, once  $P_f$  reaches the magnitude of the overburden pressure, a further increase in  $P_f$  generates vertical tension. Because the horizontal effective stress is proportional to the vertical one, as shown using Equation (3), the horizontal tension will be smaller ( $\sigma'_1$ ) than the vertical tension ( $\sigma'_3$ ) and it will increase at a lower rate. For this reason, the difference between the horizontal and vertical stresses, and therefore the size of the Mohr circle in the tensional field of the Mohr space, increases with increasing  $P_f$ . If the Mohr circle touches the failure envelope at a point on the  $\sigma_n$  axis ( $P_f = \sigma_3 + T_0$ ), a horizontal tension fracture will open (Fig. 4; Cobbold and Rodrigues, 2007). Because  $P_f$  controls the hydrofracture development similar to the pressure exerted by growing crystals ( $P_{fc}$ ) controlling the vein formation (Wiltschko and Morse, 2001; i.e. both shift the Mohr circle leftwards), it is reasonable for the magnitude of  $P_f$  to be supplemented by  $P_{fc}$  if the growth of the crystals occurs under elevated fluid pressure conditions.

## 2. Geological background

The study area is located in the Tisza Mega-unit (Haas et al., 2013, Fig. 5A), which forms the south-eastern basement of the Pannonian Basin. Many important outcrops are found in the Mecsek Mountains. The western part of the Mecsek is composed mainly of Paleozoic–Triassic sediments, including the Late Permian (Barabás-Stuhl, 1981) BCF (Fig. 5B). The distribution of the formation covers approximately 150 km<sup>2</sup>, and its maximum thickness is nearly 1000 m (Konrád and Hámos, 2006). The entire sedimentary sequence has not yet been revealed by drilling; nevertheless, the formation presents its greatest thickness (900 m) at the BAF-2 well (Fig. 6). Based on acoustic borehole televiewer observations, the average dip angle of the bedding planes in the BAF-2 well is 40° (Bernáth et al., 2014; Sámson, 2015). The BCF consists dominantly of reddish-brown albitic claystone interbedded with dolomite, siltstone and sandstone. The main rock-forming minerals are quartz, albite, illite–muscovite (dominant clay mineral), chlorite, calcite, dolomite and hematite (Árkai et al., 2000; Máthé, 2015). In certain cases, the authigenic albite content exceeds 50 wt%; this uncommon rock type is called albitolite. Mineralogical, petrographical, geochemical and sedimentological characteristics (Árkai et al., 2000; Varga et al., 2005, 2006; Varga, 2009; Konrád et al., 2010; Máthé, 2015) indicate that the formation represents a shallow, alkaline lake sediment deposited on a playa mudflat (Konrád et al., 2010). The presence of carbonate and albite pseudomorphs after halite hopper crystals (precipitated in soft sediment during desiccation periods) in the rock matrix also supports the playa mudflat origin (Máthé and Varga, 2012).

The tectonic evolution of the study area is related to the Alpine orogeny (e.g. Horváth et al., 2006; Horváth et al., 2015); however, the effects of older tectonic events cannot be excluded. Several subsequent tectonic phases are indicated during the complex evolution of the area.



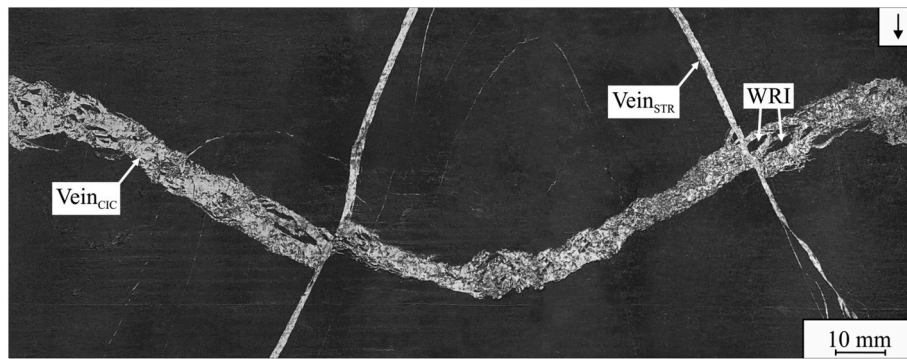


**Fig. 8.** The mutual relationship of intersecting cone-in-cone ( $\text{Vein}_{\text{CIC}}$ ) and so-called straight veins ( $\text{Vein}_{\text{STR}}$ ) in a stitched core scanner image (662.10–662.40 m TMD). The arrow in the upper right corner indicates the axis of the core samples and the down direction. WRI–wall rock inclusion.

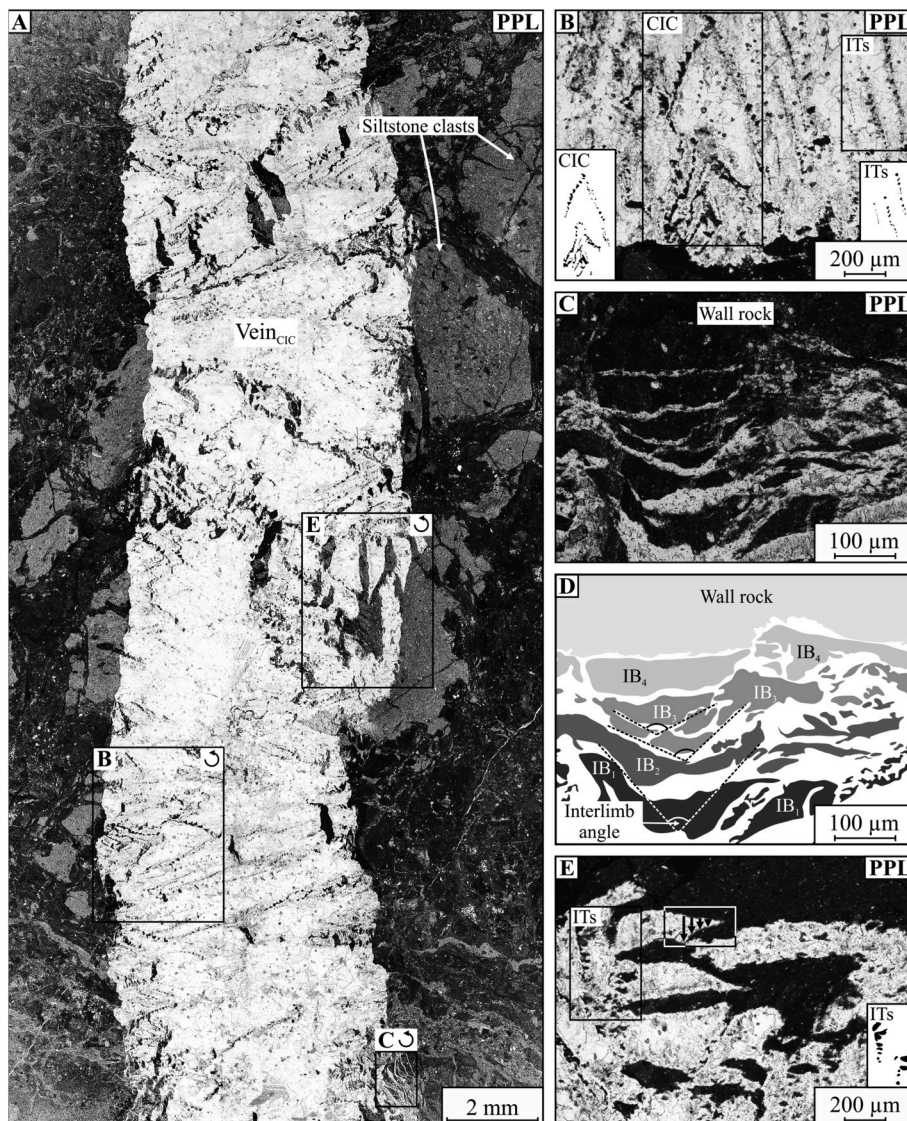


**Fig. 9.** Typical microstructure of cone-in-cone veins ( $\text{Vein}_{\text{CIC}}$ ; 251.56–251.73 m TMD). These veins contain wall rock inclusions arranged as cone-in-cone structures (CIC; B), as inclusion trails (ITs; B and E) and as inclusion bands ( $\text{IB}_{1-4}$ ; D). It should be noted that the highlighted inclusion trails (B) are missing their left ‘limbs’ to form a CIC, which can be observed in Figure A. The interlimb angle of the inclusions decreases piece by piece from the vein walls towards the centre of the vein (C and D). Figure D is the digitalised and interpretation version of Figure C; darker colours indicate earlier inclusion separations from the vein wall. Relatively large WRIs are observed in the vicinity of trails consisting of small inclusions (E). Incompletely detached wall rock fragments are inclined from the vein walls towards the central part of the vein (E). The incomplete detachment process of a WRI is indicated by black arrows surrounded by black and white rectangle. PPL–plane-polarised light.

The most important among these are the Late Cretaceous NE–SW shortening (Benkovics et al., 1997), tensional stresses and rotations in the Early Miocene (synrift phase of the Pannonian Basin; Beregart and Csontos, 1988; Csontos and Beregart, 1992; Fodor et al., 1999; Maros et al., 2004), (post-)Sarmatian compression (Sebe, 2017), post-rift thermal subsidence (Csontos et al., 2002; Maros et al., 2004) and

ongoing basin inversion, which started in the Late Pannonian (Csontos et al., 2002; Konrád and Sebe, 2010).

Interpretation of veins as evidence of multiple tectonic and/or diagenetic processes was considered in detail by Árkai et al. (2000), Lenti et al. (2010), Hrabovszki et al. (2017) and Tóth et al. (2018). Based on their macroscopic appearance, mineral-filled structural elements in



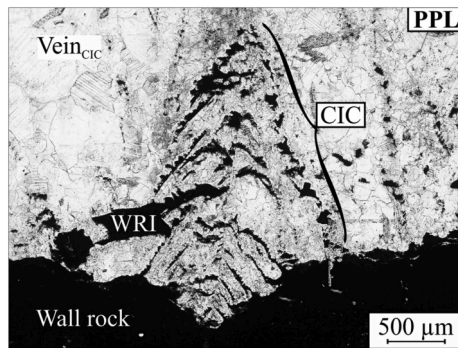


**Fig. 10.** Cone-in-cone (CIC) microstructure composed of WRIs observed in the Vein<sub>CIC</sub> (251.56–251.73 m TMD). PPL–plane-polarised light.

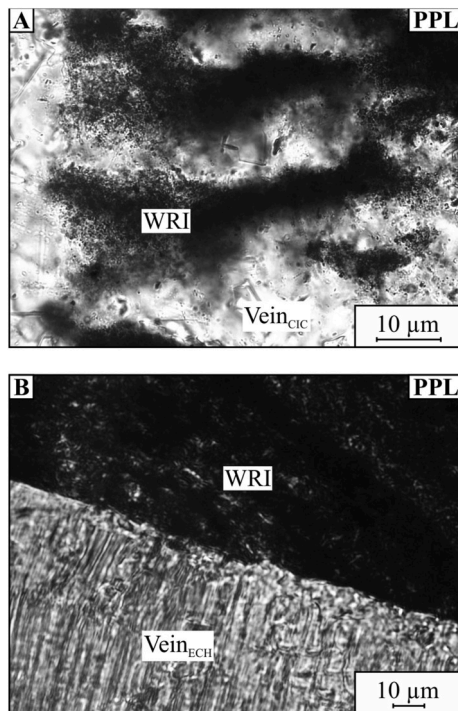


**Fig. 11.** A–Wall rock inclusions (WRI) with diffuse boundaries in Vein<sub>CIC</sub> (251.56–251.73 m TMD). B–WRI with sharp boundaries in an en-echelon vein (Vein<sub>ECH</sub>; 283.90–284.14 m TMD). PPL–plane-polarised light.

the BAF–2 well have been classified into the following categories: branched veins with WRIs, straight veins, en-echelon vein arrays and cemented breccias. In the BAF–2 well, the average dip of the veins appropriate for measurement is 42° (branched veins), 70° (straight veins) and 22° (en-echelon vein arrays). Based on cement minerals, calcite-, anhydrite-, calcite–barite- and barite–quartz-dominated veins have been distinguished; however, the proportion of these minerals varies between individual samples and locations. Based on fluid inclusion microthermometric properties and stable isotopic compositions, the parent fluids are known to be of meteoric (~70 °C; calcite-dominated veins) and hydrothermal (~150 °C; barite–quartz-dominated veins) origins (Árkai et al., 2000; Lenti et al., 2010). Vein growth can be characterised by syn-, anti- and ataxial mechanisms (details in Hrabovszki et al., 2017). Measuring primary aqueous fluid inclusions, K. Török (unpublished data) obtained eutectic temperatures ( $T_e$ ) of –23.5 °C and –39.0 °C, and a minimum final melting temperature ( $T_m$ ) from anhydrite-dominated veins of –17.7 °C, which corresponds to high-salinity (20.8 mass% NaCl<sub>eq</sub>) H<sub>2</sub>O–NaCl–CaCl<sub>2</sub> solutions, whereas

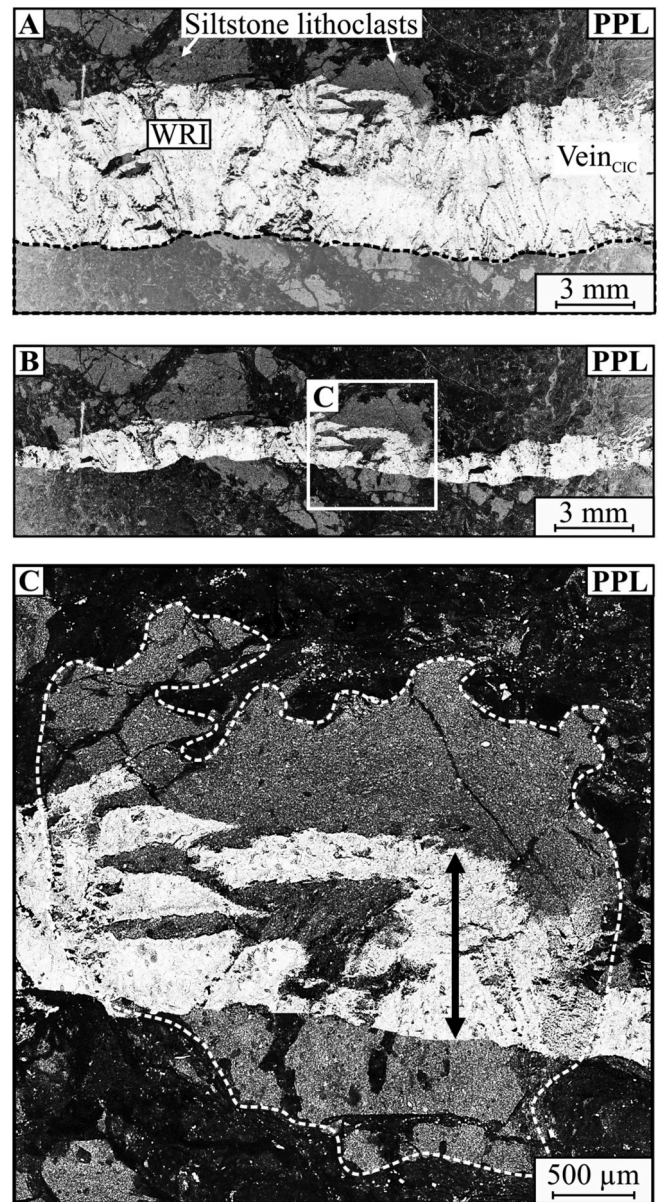


**Fig. 12.** A–Light-coloured siltstone lithoclasts on both walls of the Vein<sub>CIC</sub> (251.56–251.73 m TMD). The detached parts of the host rock (WRI) can be matched across the whole vein in such a way that the lighter shaded area marked with a black dashed line correlates with the opposite vein wall. B–As a result, the vein walls fit almost perfectly together. C–The former, pre-fragmentation shape of the siltstone lithoclast is marked out with a white dashed line. Based on these observations, the direction of the opening can be defined, as indicated by the thick black arrow. PPL–plane-polarised light.

Lenti et al. (2010) determined homogenisation temperature of ~105 °C for barite–calcite veins, which were precipitated from low-salinity fluids (3.2–4.3 mass% NaCl<sub>eq</sub>).

### 3. Methods

The petrographic description of samples was performed on polished thin sections of 30-µm thickness, using an Olympus BX41 microscope equipped with an Olympus DP73 digital microscope camera. Cathodoluminescence (CL) images were obtained using a Reliotron VII CL instrument operating at 7 kV and 0.7 mA, mounted on an Olympus BX43 microscope. Raman spectroscopy was carried out using a Thermo Scientific DXR Raman microscope equipped with a 532-nm wavelength Nd:



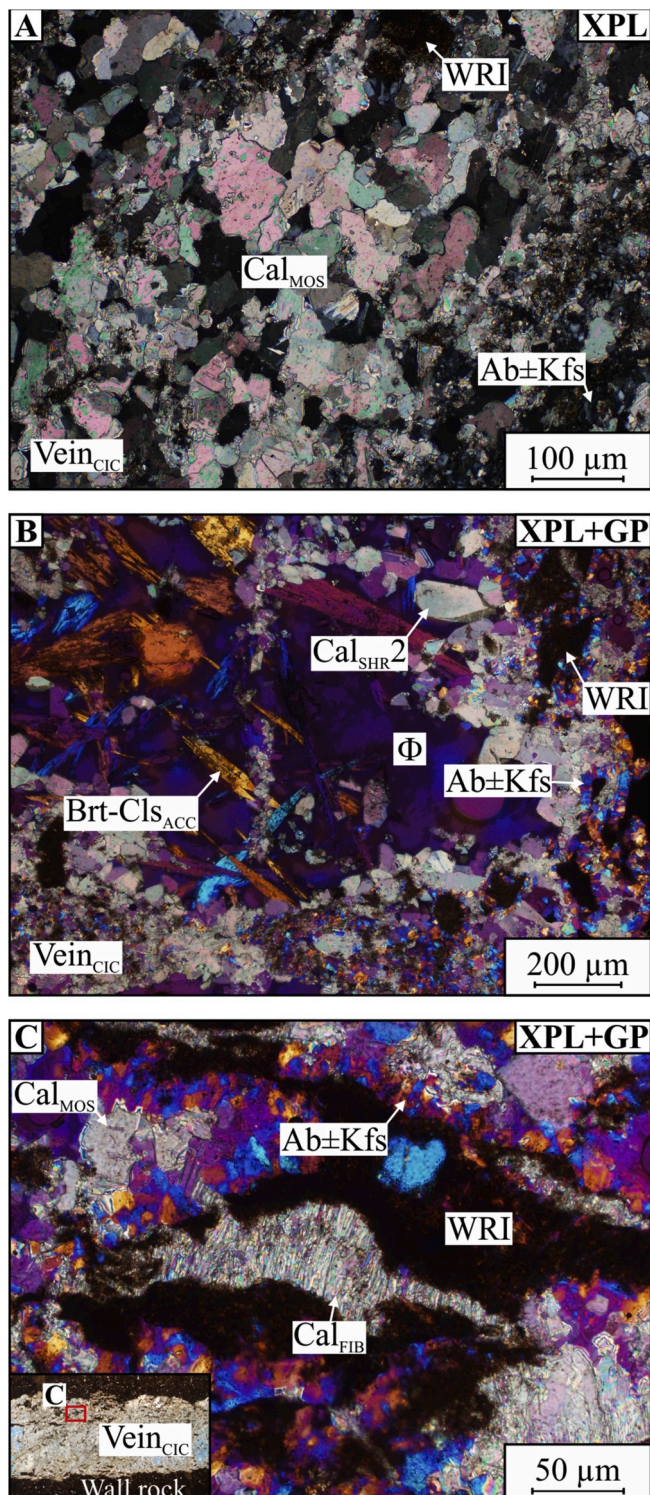


**Fig. 13.** Minerals and their microtextures in the Vein<sub>CIC</sub> (622.80–622.97 m TMD). A–Mosaic calcite (Cal<sub>MOS</sub>) texture of anhedral crystals with amorphous, interpenetrating grain boundaries. Wall rock inclusions (WRI) and fine-grained feldspar (Ab ± Kfs) crystals can also be observed. B–Acicular barite–celestine (Brt–Cls<sub>ACC</sub>) crystals within a pore (Φ) and subhedral calcite (Cal<sub>SHR2</sub>) crystals along the pore walls with surrounding WRIs and feldspar crystals. C–Fine-grained feldspar lining WRIs among mosaic and fibrous calcite (Cal<sub>FIB</sub>) grains. The red rectangle indicates the position of Figure 9C within the Vein<sub>CIC</sub>. XPL–crossed-polarised light; GP–gypsum plate. (For interpretation of the references to colour in this figure legend, the reader is referred to the Web version of this article.)

YAG laser. A laser power of 10 mW and pinhole confocal aperture of 25 µm were used for each measurement. Micro X-ray fluorescence (µXRF) mapping was performed on a Horiba Jobin Yvon XGT-5000 X-ray fluorescent spectrometer equipped with Rh X-ray source operating at 30 kV and 0.5 mA. Polarisation and CL microscopic observations, as well as the µXRF and Raman analyses, were performed at the Department of Mineralogy, Geochemistry and Petrology, University of Szeged. Scanning electron microscopic and energy-dispersive X-ray spectroscopic analyses were conducted using a Hitachi S-4700 field emission scanning electron microscope equipped with a Bruker (Röntec) QX2 energy-dispersive X-ray fluorescence spectrometer operating at 15–20 kV and 10 µA, at the Faculty of Science and Informatics, University of Szeged.

#### 4. Sample description

Drill core samples from the BAF-2 well are available for interval between depths of 251.56–831.30 m within the total measured depth (TMD). They represent claystone interbedded with siltstone and sandstone. Meso- and micro-scale observations were performed on a total of 30 drill core samples (Fig. 6).

##### 4.1. Host rock

The highly homogeneous, reddish-brown host rock contains only a few sedimentary textural elements; in most cases, even bedding planes cannot be distinguished. Sedimentary structures, such as parallel laminations or fluid-escape structures, are observable only in sandstone interbeddings (Fig. 7). Our petrographic observations are thus consistent with previous studies (Árkai et al., 2000; Máthé, 2015) in as much as the main rock-forming minerals are authigenic feldspars (both plagioclase and K-feldspar), clay minerals, carbonate minerals, hematite and detrital quartz (±feldspars and micas) with a range of grain sizes from silt to coarse sand. Occasionally, the authigenic feldspar and carbonate crystals appear in larger quantities within irregular to angular pores in the groundmass.

In the clayey–hematitic matrix, uneven, conchoidal fractures, branched veins enriched with CIC structures (Vein<sub>CIC</sub>, the subject of the present study), straight veins (Vein<sub>STR</sub>), en-echelon vein arrays consisting of sigmoidal tension gashes (Vein<sub>ECH</sub>) and cemented breccias can be observed (Hrabovszki et al., 2017). Although the absolute age of the veins is unknown, the Vein<sub>CIC</sub> is probably the oldest based on its cross-cutting relations (Fig. 8).

##### 4.2. Microstructures and vein-filling minerals of the Vein<sub>CIC</sub>

The maximum aperture of the Vein<sub>CIC</sub> is 15 mm in the observed core samples. The most characteristic feature of these veins is that they contain a high amount of WRIs (Fig. 9). In this study, the terms ‘solid inclusion’ and ‘host rock fragment’ are used interchangeably with ‘wall rock inclusion’. WRI reach lengths of up to 10 mm and a maximum width of 2 mm. They have a curved, elongated shape and commonly form both inclusion trails (Fig. 9B) and inclusion bands (Fig. 9C and D). Occasionally, solid inclusions of extremely variable sizes can be observed in adjacent spatial configurations (Fig. 9E). Furthermore, WRIs frequently occur in such unique arrangements as nested cones pointed towards the centre of the veins (CIC; Figs. 9B and 10). Each cone consists of individual, regularly spaced host rock fragments. In some cases, solid inclusions are partially split off from the vein walls and fold slightly towards the central part of the vein (Fig. 9E). The rims of solid inclusions are mostly diffuse (Fig. 11). Occasionally, on both vein walls, siltstone lithoclasts, located exactly opposite one another, can be observed with a lighter, reddish-yellow colour. The adjacent parts of these lithoclasts can be matched, as is the case for the vein walls (Fig. 12).

The major vein-forming mineral phase is calcite; however, smaller quantities of feldspar, barite–celestine, anhydrite, chlorite, pyrite–chalcopyrite and galena can also be observed. Based on



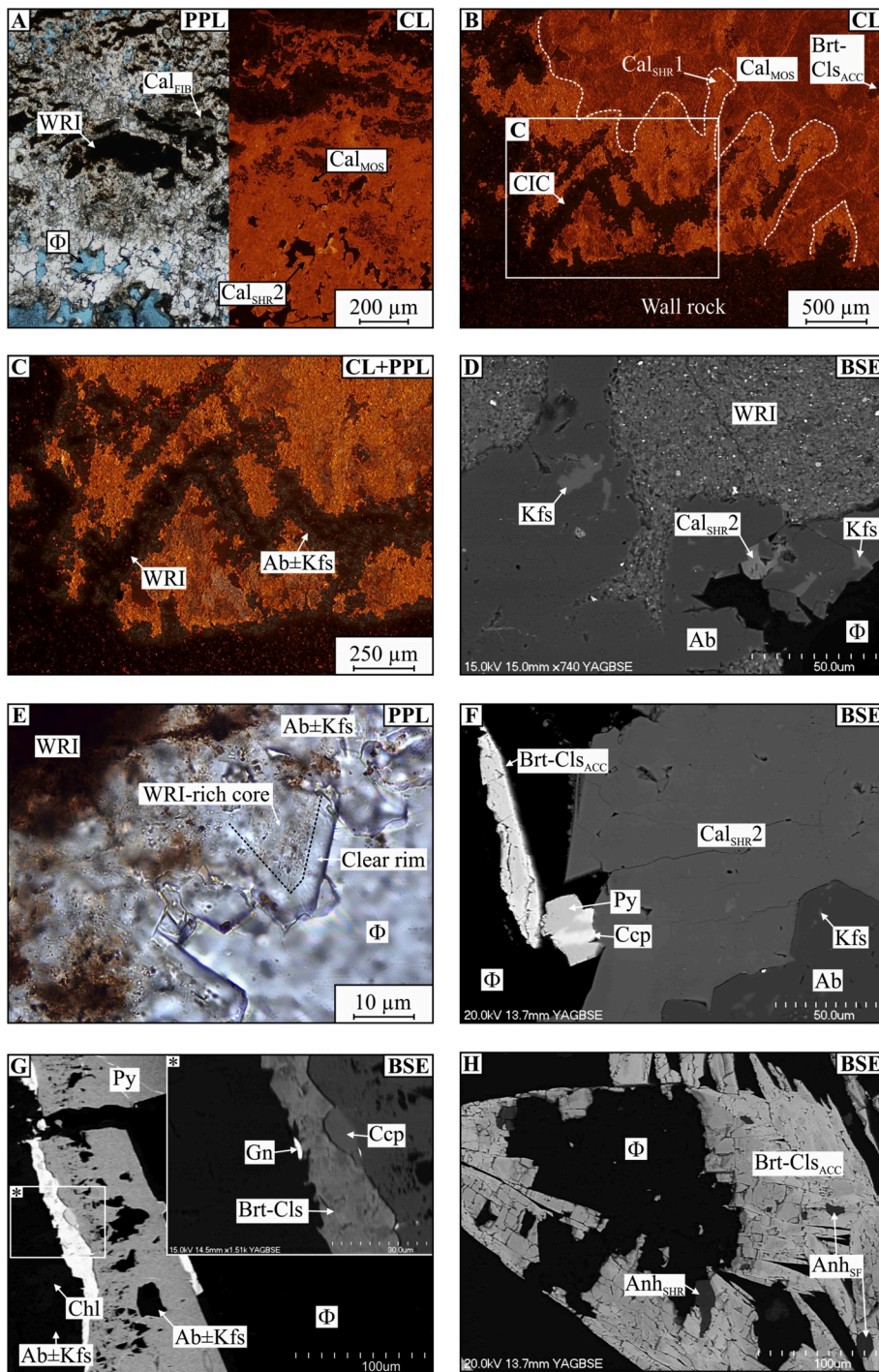


**Fig. 14.** Minerals and their microtexture in the Vein<sub>CIC</sub> from 622.80 to 622.97 m (A, D–G); from 251.56 to 251.73 m (B, C) and from 831.14 to 831.30 m (H) TMD. The fibrous calcite (Cal<sub>FIB</sub>) between wall rock inclusions (WRI), the mosaic calcite (Cal<sub>MOS</sub>) and the subhedral calcite (Cal<sub>SHR2</sub>) crystals along the pore (Φ) walls exhibit uniform orange cathodoluminescence (CL) colour (A). Different CL characteristics in the calcite phase (Cal<sub>SHR1</sub>; B, C) occur around the WRIs and along vein walls with a relatively bright orange CL colour. The straight grain boundaries of this phase are indicated by white dashed lines in Figure B. Feldspar (Ab ± Kfs) rims around the WRIs arranged as cone-in-cone (CIC) microstructures exhibit no detectable CL colour, as observed in Figure C. Feldspar rims around WRIs contain a small amount of K-feldspar (Kfs) and calcite of subhedral morphology (Cal<sub>SHR2</sub>) in addition to albite (D). The grains of the rims have solid inclusion-rich cores followed by clear mineral zones; the boundary between the two zones is indicated by black dashed lines (E). The pores are surrounded by subhedral calcite crystals (Cal<sub>SHR2</sub>), and there are acicular barite–celestine (Brt-ClS<sub>ACC</sub>) crystals associated with euhedral pyrite–chalcopyrite (Py-Ccp) grains (F). In certain cases, small domains of galena (Gn) can be observed in association with Brt-ClS<sub>ACC</sub> and Py-Ccp crystals. In order to emphasise the presence of Gn, the contrast–brightness parameters were modified during image acquisition of the inset (G). Within intracrystalline pores of the barite–celestine crystals, subhedral (Anh<sub>SHR</sub>) and space-filling anhydrite (Anh<sub>SF</sub>) phases can be observed (H). PPL–plane-polarised light; BSE–backscattered electron. (For interpretation of the references to colour in this figure legend, the reader is referred to the Web version of this article.)

microtexture, the calcite phase can be classified into three categories: mosaic, subhedral and fibrous calcite. 1) Mosaic calcite has a polycrystalline structure (Dong et al., 1995; Cal<sub>MOS</sub>; Fig. 13A). Its anhedral crystals of ~30-μm size have amorphous, interpenetrating grain boundaries mostly close to the vein walls. 2) Subhedral calcite grains are located along the vein walls (Cal<sub>SHR1</sub>) and on the pore walls (Cal<sub>SHR2</sub>; Fig. 13B). Grain sizes vary between 20 and 170 μm. 3) Fibrous calcite crystals have high (>10) length/width ratios (Cal<sub>FIB</sub>; Fig. 13C), and the length of individual fibres is between 7 and 90 μm. Most carbonate phases (Cal<sub>MOS</sub>, Cal<sub>SHR2</sub>, Cal<sub>FIB</sub>) show dull orange cathodoluminescent (CL) colours (Fig. 14A), however, the Cal<sub>SHR1</sub> phase exhibits a distinct, relatively bright orange CL colour (Fig. 14B and C).

Feldspar occurs in unique textural positions as a thin selvage zone on the vein walls and around WRIs (Fig. 14C). This rim is composed of subhedral albite and K-feldspar grains, where albite is dominant (Ab ± Kfs; Fig. 14D). The μXRF maps presented in Fig. 15 show the occurrence of the feldspar cement around WRIs within the Cal<sub>SHR1</sub> calcite mineral phase. Albite crystals range in size up to around 30 μm. Frequently, these crystals show zoned microfabrics. The clear rims of the crystals surround darker, solid inclusion-rich cores (Fig. 14E). The feldspar cement often encloses pyrite–chalcopyrite (Py-Ccp) grains and chlorite (Chl) flakes. Barite–celestine crystals associated with euhedral pyrite–chalcopyrite crystals of 25-μm size (Fig. 14F) and small galena grains (Fig. 14G) are located within pores of 50-μm to 3-mm size. In most cases, these crystals



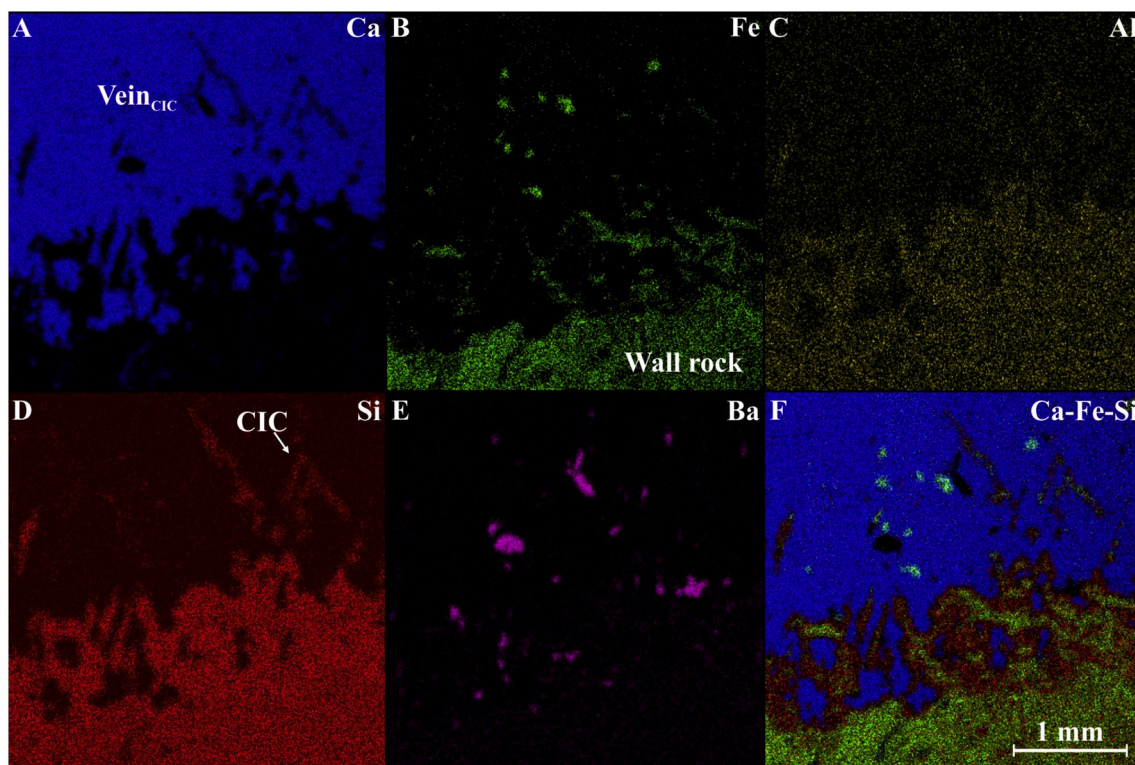


**Fig. 15.** Representative element distribution across a Vein<sub>CIC</sub>-wall rock boundary zone. Micro X-ray fluorescence (μXRF) maps show the distributions of Ca, Fe, Al, Si and Ba within the selected boundary domain. Due to the co-occurrence or anti-correlation of certain elements, a quasi-phase distribution map was constructed using the Ca-Fe-Si element maps sandwiched together (F). From this composite image, it is obvious that cone-in-cone domains of the Vein<sub>CIC</sub> consist of WRIs surrounded by albite ± K-feldspar rim (251.56–251.73 m TMD).

have an acicular habit (Brt-Cl<sub>s</sub><sub>ACC</sub>; Fig. 13B) and lengths from 50 to 550 μm. Barite-celestine is also associated with the dull orange CL Cal<sub>MOS</sub> phase (Fig. 14B). Dissolved portions of barite-celestine crystals can be partially (or completely) cemented with 5–15-μm subhedral to anhedral anhydrite crystals (Anh<sub>SHR</sub>; Fig. 14H). In some cases, this anhydrite phase also fills the remaining pore space (Anh<sub>SF</sub>).

## 5. Discussion

### 5.1. Possible formation mechanisms of the Vein<sub>CIC</sub>

The geometries of individual WRIs within inclusion bands, inclusion trails and CIC microstructures, as well as the occurrence of fibrous crystals (Figs. 1, 9 and 13C), allows the proposition of two different vein formation mechanisms: a) crack-seal process or b) continuous vein growth (Means and Li, 2001; Wiltshko and Morse, 2001; Hilgers and Urai, 2005; Cobbold and Rodrigues, 2007; Cobbold et al., 2013). Most individual WRIs within the veins have folded shapes (Fig. 9). Some connect to vein walls with thin necks and bend towards the centre of the veins (Fig. 9E). These solid inclusions are surrounded by vein-filling minerals, suggesting that partial separation of the WRIs occurred coevally with vein mineralisation. Moreover, if these WRIs had deformed after vein formation, they should have bent uniformly and would show identical shapes. This has not been observed in our samples; the inclusions instead exhibit various grades of deformation. According to these observations, the solid inclusions have folded and detached from vein walls simultaneously with the opening of the veins.

The interlimb angle of the folded WRIs decreases gradually from the vein walls towards its central zone (Fig. 9C and D). Such continuous solid inclusion deformation (Fig. 9C–E) is problematic to be explained by the crack-seal mechanism. Considering that many small inclusions are the result of small opening increments, whereas relatively large inclusions indicate larger openings, the adjacent emergence of inclusions

with very different sizes (Fig. 9E) also cannot be explained by the crack-sealing mechanism.

Based on the fold geometry of WRIs, the presence of CIC microstructures, and the partial separation of solid inclusions from the vein walls, the generation of the solid inclusions appears to be related to continuous deformation (Rutter, 1986; Fossen and Cavalcante, 2017) instead of the episodic crack-seal mechanism. Diffuse WRI boundaries (Fig. 11) suggest that the sediment was poorly consolidated during vein development and that the force of crystallisation was capable of breaking fragments away from the vein walls, deforming them continuously during the detachment process and separating the WRIs into individual solid inclusion grains. As there are no signs of plastic deformation (e.g. undulose extinction, deformation twinning or low-temperature grain boundary migration of detrital quartz and feldspars) of WRIs, the mechanism of ductile-style deformation is presumably brittle (frictional), which typically occurs in poorly consolidated porous rocks and sediments (Fossen, 2010).

In summary, continuous vein growth appears to have been the most important mechanism of vein formation and satisfactorily explains the formation of characteristic WRI arrangements and the folded shape of the solid inclusions (Hilgers and Urai, 2005). The ductile-style deformation of the WRIs (and the vein formation itself) possibly occurred within a low-cohesion sediment.

### 5.2. Interpretation of microstructures and crystal morphologies in the Vein<sub>CIC</sub>

As shown above, curved solid inclusions or inclusion trails, inclusion bands and CIC-like arrangements of WRIs (Figs. 9 and 10) suggest continuous vein growth mechanism. Continuous deformation results in the constant growth of crystals, or *vice versa*: the constant growth of crystals causes continuous deformation. Owing to the constant growth and lack of open space during crystallisation, growth competition

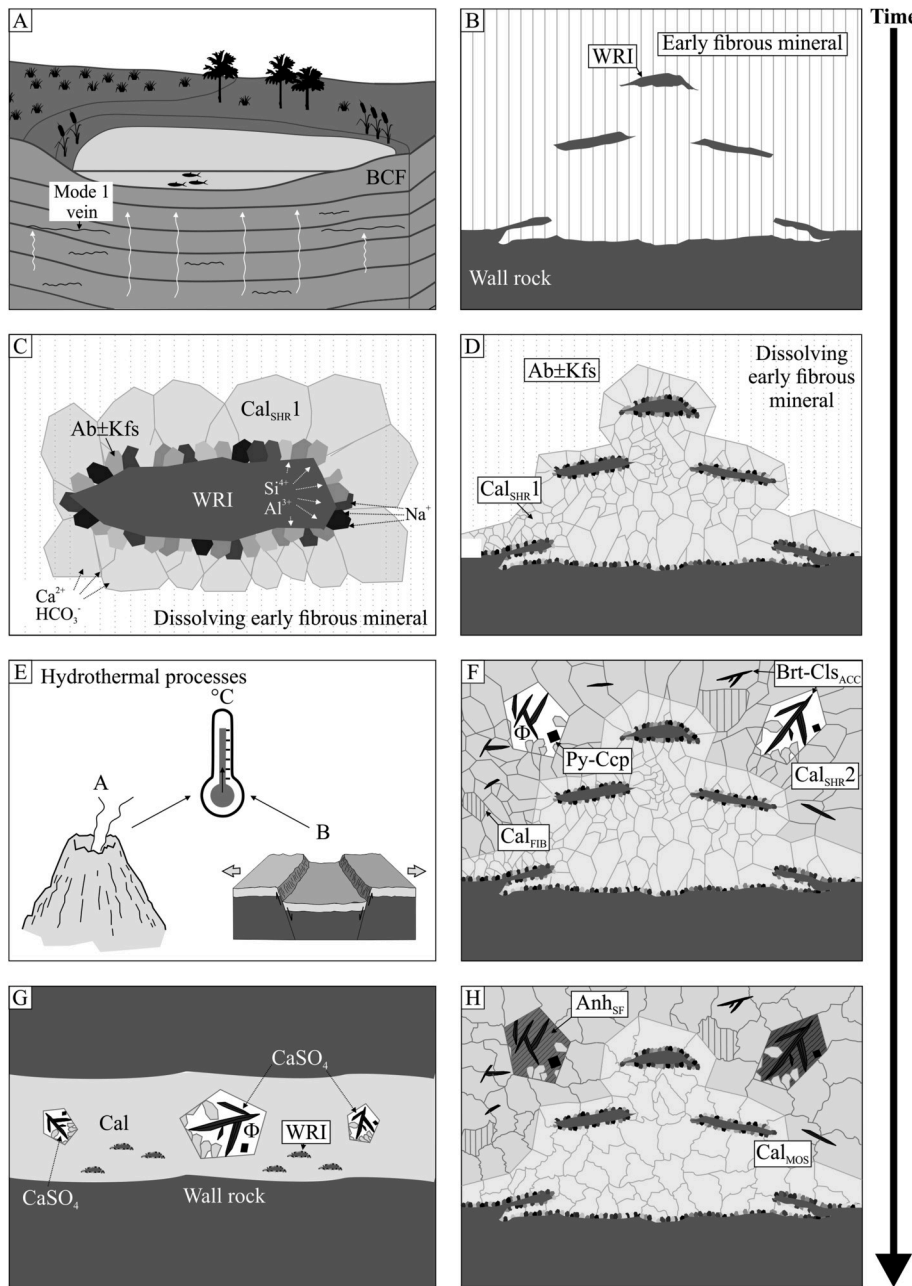


**Fig. 16.** The potential evolution of the CIC-containing veins in the Boda Claystone Formation (BCF). A and B—Due to compaction, pressure solution, vertical fluid movement and force of crystallisation, veins were formed in the siliciclastic sediment. During the continuous vein formation process, fragments were detached from the wall rock (WRI) and cemented by fibrous crystals. C and D—In a later stage of vein evolution, the early fibrous mineral phase simultaneously dissolved with the precipitation of feldspar ( $\text{Ab} \pm \text{Kfs}$ ), chlorite, pyrite–chalcocopyrite and calcite ( $\text{Cal}_{\text{SHR1}}$ ) around the WRIs and along the vein walls. Possible sources of  $\text{Si}^{4+}$  and  $\text{Al}^{3+}$  are clay minerals and detrital feldspar. The source of  $\text{Na}^+$  is potentially the dissolving early fibrous mineral or hopper halite crystals in the wall rock, whereas  $\text{Ca}^{2+}$  could have arrived from dissolved evaporite minerals in the wall rock and/or from detrital plagioclase grains. The  $\text{HCO}_3^-$  content of the pore fluid reacted with the  $\text{Ca}^{2+}$ , forming the calcite mineral phase. E and F—As a result of hydrothermal processes (elevated thermal activity due to magmatic processes or tectonic depression), barite–celestine ( $\text{Brt-ClS}_{\text{ACC}}$ ) and pyrite–chalcocopyrite  $\pm$  galena ( $\text{Py-Ccp}$ ) precipitated syngenetically with younger calcite ( $\text{Cal}_{\text{SHR2}}$ ;  $\text{Cal}_{\text{FIB}}$ ) phases. G and H—During the last evolution stage, anhydrite ( $\text{Anh}_{\text{SF}}$ ) filled the remaining pores of the veins and in certain cases replaced the barite–celestine and calcite phases. A potential source of anhydrite is the dissolution of evaporite minerals from the wall rock.

between the crystals is suppressed and crystals precipitate with fibrous morphology (Bons, 2000; Hilgers et al., 2001). The fibrous habit does not depend on the chemical composition and specific crystal structure of minerals (Passchier and Trouw, 2005).

The observed fibrous calcite crystals ( $\text{Cal}_{\text{FIB}}$ ) with smooth grain boundaries can be associated with continuous vein growth (Hilgers and Urai, 2005; Bons et al., 2012). However, based on textural relations (e.g. gradual transition from fibrous to mosaic grains; Figs. 13C and 14A) and uniform CL characteristics (Fig. 14A and B), the  $\text{Cal}_{\text{FIB}}$  is cogenetic with  $\text{Cal}_{\text{SHR2}}$  and associated mineral phases, which were formed after the  $\text{Ab} \pm \text{Kfs}$ ,  $\text{Chl}$ ,  $\text{Py-Ccp}$  and  $\text{Cal}_{\text{SHR1}}$  crystals postdating the formation of CIC structures. Consequently,  $\text{Cal}_{\text{FIB}}$  is presumably not synkinematic with the development of the vein microstructure. Thus, it is necessary to hypothesise an early fibrous phase that is no longer present in the veins.  $\text{Cal}_{\text{FIB}}$  is potentially the pseudomorph of this earlier, fibrous mineral phase that characterised the entirety of the vein before replacement processes occurred. Based on these considerations, vein development

can be divided into four stages:

- (1) WRIs were detached from the vein walls (Fig. 9C, D, E), and CIC microstructures were formed (Figs. 9B and 10) because of growing fibrous crystals that filled the veins completely (Fig. 16A and B).
- (2) Fibrous crystals were replaced (Fig. 16C and D) by albite  $\pm$  K-feldspar (Fig. 14D, G), chlorite, pyrite–chalcocopyrite ( $\text{Py-Ccp}$ ; Fig. 14G) and subhedral calcite ( $\text{Cal}_{\text{SHR1}}$ ) crystals (Fig. 14B and C). The relatively early, cogenetic precipitation of these minerals is evidenced by their close contact with WRIs and textural relations.
- (3) The subhedral ( $\text{Cal}_{\text{SHR2}}$ ) and fibrous calcite ( $\text{Cal}_{\text{FIB}}$ ; Fig. 13C) with dull orange CL colour (Fig. 14A), associated with acicular barite–celestine ( $\text{Brt-ClS}_{\text{ACC}}$ ),  $\text{Py-Ccp}$  and galena ( $\text{Gn}$ ; Fig. 14F and G) precipitated on  $\text{Cal}_{\text{SHR1}}$  crystals (Fig. 14B) replacing the remaining fibrous vein-filling crystals (Fig. 16E and F).



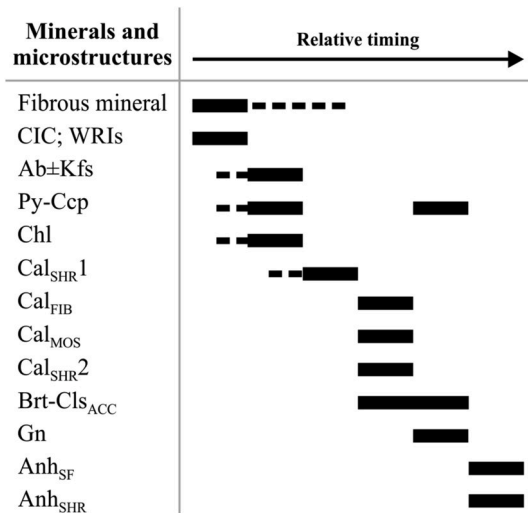


Fig. 17. Paragenetic sequence of the observed and inferred microstructures and vein-filling minerals based on textural relations.

- (4) Anhydrite crystals filled any remaining pore spaces ( $Anh_{SF}$ ; Fig. 16G and H) and partially replaced  $Brt-Cls_{ACC}$  crystals ( $Anh_{SHR}$ ), as observed on subhedral anhydrite crystals within secondary intracrystalline pores of  $Brt-Cls_{ACC}$  (Fig. 14H).

Feldspar crystals may have precipitated in  $Vein_{CIC}$  as a result of albitisation, a process known to have affected the entire BCF during its early diagenetic evolution (Árkai et al., 2000; Varga et al., 2005). The small WRI particles observed within feldspar crystals (Fig. 14E) suggest that the sediment was still not fully consolidated during this process.

K. Török (unpublished data) determined the minimum final melting temperatures ( $T_m$ ) of  $-17.7^\circ\text{C}$  and eutectic temperatures ( $T_e$ ) of  $-23.5^\circ\text{C}$  and  $-39.0^\circ\text{C}$  for primary fluid inclusions in anhydrite–calcite veins of the BCF, which were precipitated from high-salinity (20.8 mass%  $NaCl_{eq}$ )  $H_2O-NaCl-CaCl_2$  solution. Because the presence of an early halite phase in the BCF is proved by pseudomorphs after hopper halite crystals (Máthé and Varga, 2012) and the salinity of the fluid inclusions in the vein-forming calcite phase is relatively high, it is possible that the hypothetical early fibrous phase was a highly soluble salt. However, no direct evidence is available, and the high salinity of the fluid inclusions may result from other sources, such as the dissolution of the mentioned hopper crystals or migration of brine along the fractures.

Land and Prezbindowski (1981) proposed a reaction for the origin of saline water in carbonates, which may be responsible for the dissolution of the early halite phase and the precipitation of an albite phase in the  $Vein_{CIC}$ , namely, halite + detrital plagioclase + quartz + water  $\rightarrow$  albite +  $Na-Ca-Cl$  brine.

The mosaic texture (or ‘jigsaw-puzzle’ structure) of calcite was probably formed during the recrystallisation of  $Cal_{FIB}$  and  $Cal_{SHR2}$  crystals (Fig. 16H; Lovering, 1972; Dong et al., 1995). Based on both the euhedral appearance of  $Py-Ccp$  crystals and the presence of  $Gn$ , the third vein-forming stage could be related to hydrothermal processes (Fig. 16E). A potential Late Triassic–Jurassic sulphidic hydrothermal mineralisation in Permian and Early Triassic lithologies of this region was reported by Fazekas and Vincze (1991), specifically in the southern foreland of the BAF–2 well.

The paragenetic sequence of the observed and inferred vein-filling minerals in the  $Vein_{CIC}$  is detailed in Fig. 17.

### 5.3. Orientation and failure mode of the $Vein_{CIC}$

In some drill core samples, the members of  $Vein_{CIC}$  generation are observed to be sub-parallel (difference  $< 5^\circ$ ) to bedding. Nevertheless, in

most cases, the bedding cannot be determined at macroscopic scales. According to acoustic borehole televiewer observations in the BAF–2 well, the average dip angle of the strata is  $40^\circ$  (Bernáth et al., 2014; Sámson, 2015), which is roughly equal to the average  $42^\circ$  dip angle of the  $CIC$ -containing veins (Hrabovszki et al., 2017). This suggests that the investigated veins formed nearly parallel to bedding; thus, the original direction of the vein planes was horizontal.

Based on the orientation of solid inclusion trails and  $CIC$  microstructures (Figs. 9 and 10), and furthermore, on the relative position of lithoclasts on the vein walls (Fig. 12),  $Vein_{CIC}$  can be characterised as cemented Mode I type fractures (e.g. Twiss and Moores, 1992; Van der Pluijm and Marshak, 2004; Fossen, 2010). Accordingly, vein widening occurred perpendicular to the vein walls and under negligible shear stress. The fracture plane was parallel to the maximum effective stress ( $\sigma'_1$ ) and perpendicular to the minimum effective stress ( $\sigma'_3$ ) directions. Under these circumstances, tensional fractures may develop such that the Mohr circle touches the failure envelope only at one point on the  $\sigma_n$  axis in the tensional field of the Mohr space. For this situation, the effective and differential stresses ( $\sigma_d$ ) must be relatively low. Low effective stresses can exist in the case of elevated  $P_f$  and/or elevated  $P_{fc}$ , whereas small  $\sigma_d$  is generally found near the surface according to Equation (6):

$$\sigma_d \approx 0.5 \rho \cdot g \cdot h, \quad (6)$$

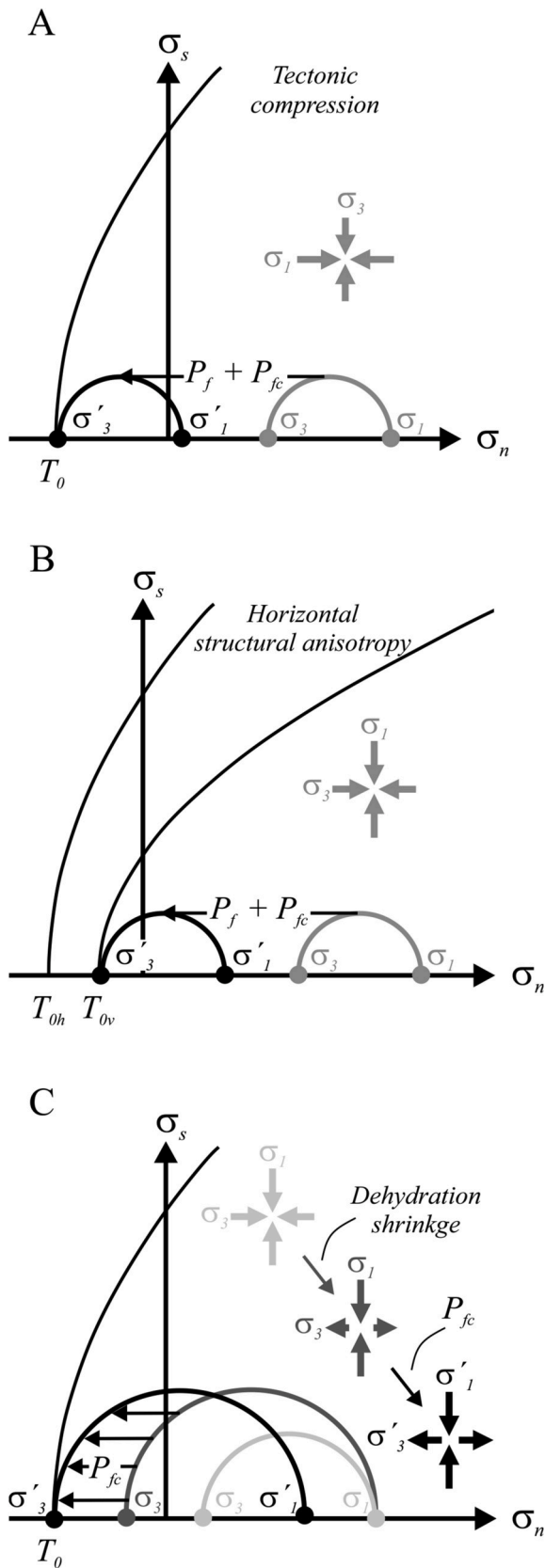
where  $\rho$  is density (representative crustal value of  $2700 \text{ kg/m}^3$ ),  $g$  is acceleration due to gravity ( $9.8 \text{ m/s}^2$ ) and  $h$  is depth (Van der Pluijm and Marshak, 2004). Small  $\sigma_d$  can also be achieved in deeper environments owing to seepage forces (details in Chapter 1.2.).

According to Gale et al. (2014), in addition to seepage force mechanism (Fig. 4), tectonic stresses (Fig. 18A) and tensile strength anisotropy (e.g. bedding planes; Fig. 18B; Lash and Engelder, 2005) may engender bedding-parallel vein orientation if elevated  $P_f$  and/or  $P_{fc}$  are present. Stress reduction (tectonic uplift; El Tabakh et al., 1998), hydrocarbon generation during catagenesis (Rodrigues et al., 2009), compaction (Terzaghi et al., 1996), crystallisation pressure (Taber, 1916; Meng et al., 2018a) and dehydration shrinkage (Fig. 18C; Plummer and Gostin, 1981), as well as their combinations, can also contribute to vein development (Table 1). The high pore fluid supersaturation required for significant crystallisation pressures can result from evaporation close to the surface (Means and Li, 2001; Wiltchko and Morse, 2001) or pressure solution at higher burial depths (Fowler and Yang, 1999; Yang, 2000; Meng et al., 2018b).

Considering that the presently investigated vein generation is the earliest one in the BAF–2 well (Fig. 8; Hrabovszki et al., 2017) and that it was potentially formed within a poorly consolidated sediment by continuous vein opening with contemporaneous crystallisation (details in Chapter 5.1.), it is plausible that  $CIC$  veins formed in a tectonically inactive environment. Hydrocarbon generation during catagenesis can also be ruled out because solid and liquid hydrocarbon residues have not been detected in the BCF.

### 5.4. Processes responsible for continuous vein formation

Based on microstructural observations (e.g. WRI geometries, arrangements, boundaries) it can be concluded that  $Vein_{CIC}$  was formed by continuous vein growth processes. During vein formation, crystals precipitated synchronously with the opening, and crystal growth was the main reason for vein development by displacive widening. Previous theories explain the origin of horizontal vein orientation, fibrous crystal morphology and  $CIC$  microstructure formation, but none of these models satisfactorily explains these features collectively, as is observed in the present case. For this reason, we propose two models that describe possible processes responsible for continuous vein formation along horizontal surfaces at different burial depths in the BCF:



(caption on next column)

**Fig. 18.** The influence of tectonic compression (A), horizontal structural anisotropy (B) and dehydration shrinkage (C) on the stress field and thus on the fracture orientation in the presence of elevated fluid ( $P_f$ ) and/or crystallisation pressures ( $P_{fc}$ ). A—As a result of tectonic compression, the horizontal applied stress becomes larger. The elevated  $P_f + P_{fc}$  shifts the Mohr circle to the left. If the difference between  $\sigma'_1$  and  $\sigma'_3$  is low, horizontal tensile fracture forms when the failure envelope is touched by the Mohr circle at a point on the  $\sigma_n$  axis. B—The failure envelopes pertain vertical ( $T_{0v}$ ) and horizontal ( $T_{0h}$ ) tensile strengths in the presence of horizontal structural anisotropy (e.g. bedding planes; based on Vernik, 2016). Due to increasing  $P_f$  and/or  $P_{fc}$ , the Mohr circle for effective stress touches the failure envelope for vertical tensile strength as  $T_{0v}$  is lower than  $T_{0h}$ . If the difference between  $\sigma'_1$  and  $\sigma'_3$  is low, horizontal tensile fracture forms. C—In response to the ongoing dehydration, tensile stress is exerted increasing the size of the Mohr circle, which enters the tensional field of the Mohr space. Due to  $P_{fc}$ , the Mohr circle of the same size shifts leftwards. Again, if the difference between  $\sigma'_1$  and  $\sigma'_3$  is small, tensile fracture occurs, now in the vertical direction.

- 1) Close to the surface (<15 m; Plummer and Gostin, 1981), the dehydration of sediments during evaporation and desiccation periods of the playa mudflat may lead to the concentration and supersaturation of pore fluid components. This may be supplemented by tensile stress exerted by dehydration shrinkage. The increasing saturation of the pore fluid (Means and Li, 2001; Wiltschko and Morse, 2001) and tensile stress (Plummer and Gostin, 1981) may result in mineral precipitation from the supersaturated pore fluid. As a result, subvertical microveins may develop in the sediment, because the greatest effective stress ( $\sigma'_1$ ) is vertical while the least effective stress ( $\sigma'_3$ ) is horizontal based on the overburden pressure (Fig. 18C). In the presence of horizontal weakness planes (e.g. bedding), horizontal veins may also develop, i.e. horizontally-oriented clay mineral flakes along the bedding planes may result in considerably lower tensile strength ( $T_0$ ) normal to bedding than parallel to it (Lash and Engelder, 2005). For example, tensile strength normal to bedding ( $T_{0v}$ ) in shales may be one-quarter higher than parallel ( $T_{0h}$ ) to it (Schmidt, 1977). As a result, the growing crystals must exert less pressure vertically along horizontal planes than they would grow horizontally along vertical planes, because  $\sigma_3 + T_{0v} \ll \sigma_3 + T_{0h}$  (Fig. 18B). The fibrous morphology of the crystals may result from suppressed growth competition caused by a lack of open space during crystallisation (Bons, 2000; Hilgers et al., 2001). As a result of precipitation, the saturation of the fluid decreases; however, ongoing evaporation may increase pore fluid saturation again. As long as these processes operate simultaneously (the fibrous crystals are in contact with a supersaturated solution in the wall rock pores), vein opening and crystal growth also operate simultaneously. In the BCF, carbonate and albite pseudomorphs after halite hopper crystals (Máthé and Varga, 2012) indicate desiccation periods during sediment deposition. This suggests that the conditions necessary for vein growth according to the outlined model were available. Because the average dip angle of the observed veins (Hrabovszki et al., 2017) is approximately equal to that of the bedding planes (Bernáth et al., 2014; Sámson, 2015), crystals had an opportunity to grow along these weakness planes as described above. However, the discussed veins are observed to cut across light-coloured siltstone lithoclasts (Fig. 12), which suggests that tensile strength anisotropy did not play a significant role in their formation. This indicates that their opening did not occur along the former weakness planes.
- 2) In deeper environments, due to the increasing overburden load, sediments are continuously compressed. This compression does not occur immediately but rather reaches a final value corresponding to the amount of the overburden during a relatively long timescale (Terzaghi et al., 1996). The expanding load enlarges the effective stress in the sediment (Fig. 19A). The increasing effective stress elevates the degree of pressure solution since the solubility of minerals



**Table 1**

Possible causes of bedding-parallel Mode I type fracture formation within pre-to semi-lithified sediments (based on Gale et al., 2014).

No.	Formation cause(s)	Effect on pressure	Fracture orientation	Corresponding figure	Role in the formation of studied veins
1	Tectonic compression	Increasing horizontal stress	Horizontal	Fig. 18A	–
2	Seepage forces	Minimum compressive stress becomes vertical	Horizontal	Fig. 4	+
3	Structural anisotropy (e.g. bedding planes)	Decreasing vertical $T_0$	Horizontal	Fig. 18B	–
4	Tectonic uplift	Increasing $P_f$	Vertical	Fig. 2	–
5	Catagenesis	Increasing $P_f$	Vertical	Fig. 2	–
6	Compaction	Increasing $P_f$	Vertical	Fig. 2	+
7	Crystallisation	Increasing $P_{fc}$	Vertical	Fig. 2	+
8	Dehydration shrinkage	Decreasing horizontal stress	Vertical	Fig. 18C	–

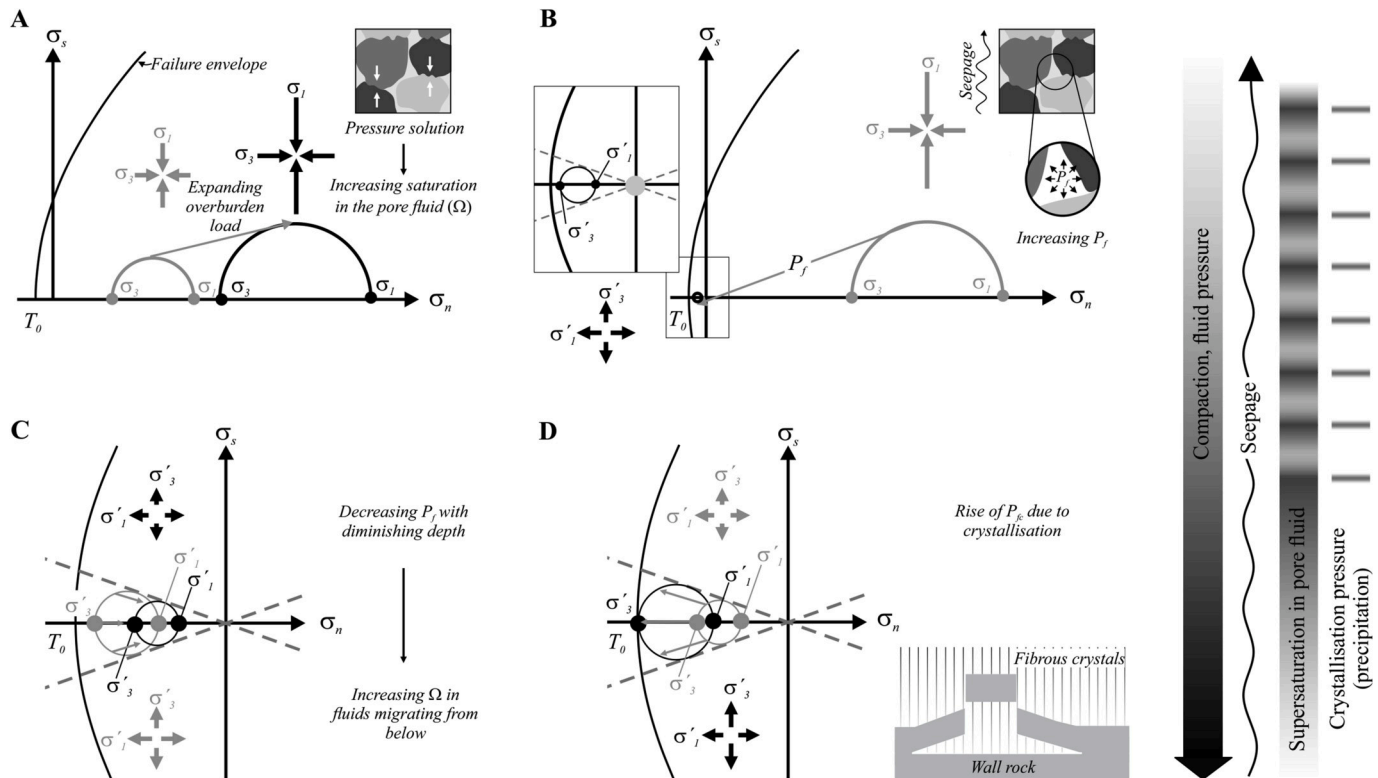


**Fig. 19.** Conceptual model of displacive vein formation along horizontal surfaces induced by the effects of pressure solution, fluid overpressure, seepage forces, and crystallisation pressure. The relevant largest and smallest principal stress values are expressed as  $\sigma_1$  and  $\sigma_3$ ; while grey colour represents the early state of the processes in the subfigures. A–Due to expanding overburden load the sediment is compressed. The size of the Mohr circle increases with the increasing greatest ( $\sigma_1$ ) and least applied stresses ( $\sigma_3$ ). At greater depths (i.e. higher stresses) minerals dissolve at grain contacts increasing the saturation in the pore fluid ( $\Omega$ ). B–As the compaction progresses, the fluid pressure ( $P_f$ ) significantly increases. Because the sediment is anisotropically compacted, a vertical gradient in the  $P_f$  induce upward fluid migration (seepage). Seepage forces act against the weight of the overburden, initially reducing the effective stresses and later engendering tensile effective stress. Accordingly, the Mohr circle shifts to the left and decreases in size. The maximum effective stress ( $\sigma'_1$ ) becomes horizontal and the minimum effective stress ( $\sigma'_3$ ) becomes vertical. C–The saturation in the upward-migrating pore fluid increases, while the size of the Mohr circle decreases with decreasing  $P_f$ . D–When the pore fluid becomes supersaturated enough, crystals precipitate. In this state, the growing crystals exert pressure ( $P_{fc}$ ) equal to  $\sigma_3 + T_0 - P_f$ . The Mohr circle touches the failure envelop at a point on the  $\sigma_n$  axis that results in the formation of horizontal veins. The supersaturation in the pore fluid decreases with crystallisation. After precipitation, the supersaturation in the upward-migrating pore fluid increases again, as shown by Figure C.

at grain contacts intensifies with increasing effective stress (e.g. Fowler and Yang, 1999; Yang, 2000). Minerals with a low stress coefficient of solubility (Weyl, 1959; Obika et al., 1992) dissolve most intensively, particularly at greater depths where the sediment is sufficiently compacted. At a later stage, the growing overburden results in developing  $P_f$ . The distribution of the  $P_f$  is not uniform in the sediment, and potential differences may cause fluid movement. Highly saturated pore fluid can be squeezed out of the underlying sediments, commonly upward as a result of vertical pressure gradients. A vertical pressure gradient can readily develop in sediments, in which the primary porosity is relatively high (>60%) but degrades

readily with growing burial depth (Dewhurst et al., 1998; Rutter et al., 2017). Because of this fluid movement, seepage forces act on the framework of the sediment (Cobbold and Rodrigues, 2007); the vertical effective stress decreases by the amount of  $P_f$  (Figs. 4 and 19B). Because there is no horizontal seepage, horizontal effective stress is unaffected; rather it correlates with the vertical effective stress as shown using Equation (3). As soon as  $P_f$  exceeds the amount of pressure generated by the overburden weight, the horizontal effective stress becomes larger than the vertical one. In other words, the greatest effective stress ( $\sigma'_1$ ) becomes horizontal and the least effective stress ( $\sigma'_3$ ) becomes vertical (Figs. 4 and 19B). The

saturation of upward-migrating pore fluids gradually increases with decreasing  $P_f$  (Fig. 19C). Once the pore fluid becomes supersaturated in a stress field where  $\sigma'_1$  is still horizontal, precipitation occurs along horizontal surfaces (Fig. 16A and B, 19D). For this type of vein growth to occur, the Mohr circle must touch the failure envelope at a point on the  $\sigma_n$  axis in the tensile field of Mohr space. Because  $P_{fc}$  acts in vein growth similarly to how  $P_f$  controls hydrofracture development (Wiltchko and Morse, 2001), this type of vein growth may occur when the sum of  $P_f$  and  $P_{fc}$  reaches the magnitude of the overburden load and tensile strength of the sediment ( $\sigma_3 + T_0$ ). Here, the effective stress ( $\sigma'$ ) is influenced by  $P_f$  and  $P_{fc}$  as shown using Equation (7):

$$\sigma' = \sigma - (P_f + P_{fc}), \quad (7)$$

where  $\sigma$  is the applied stress. If  $P_f$  decreases, the supersaturation of the pore fluid increases, and crystallisation thus applies greater pressure, and *vice versa*: increasing  $P_f$  reduces the supersaturation resulting in lower  $P_{fc}$ . This means that a continuous feedback reaction can occur, which can result in continuous vein opening and simultaneous crystallisation. The factors of this reaction ( $P_f$ ,  $P_{fc}$ ;  $\sigma'$  and fluid saturation) affect each other: while one is continually changing, the others are also continually changing. Therefore, as required for the CIC formation suggested by our petrographic observations, the Mohr circle is not shifting back and forth, causing episodic opening increments; rather, it is constantly in the tensional field of the Mohr space until this interaction occurs, which is possible until:

$$P_f + P_{fc} \geq \sigma_3 \quad (8)$$

It is important to highlight that these processes can produce horizontal (Cobbold and Rodrigues, 2007) continuously growing veins only if vertical fluid migration occurs. The reliability of this model is supported in the case of the BCF by the orientation of the veins and the presence of fluid-escape structures (Fig. 7).

## 6. Conclusions

The growth of the studied vein generation (Vein<sub>CIC</sub>) in the Late Permian BCF was continuous, as evidenced by (1) the folded WRI geometries; (2) the decreasing interlimb angle of the folded WRIs towards the centre of the veins; (3) the partial separation of solid inclusions from the vein walls; and (4) the side-by-side emergence of WRIs with distinct sizes. Displacive vein growth was potentially controlled by the pressure generated by growing crystals (Means and Li, 2001; Wiltchko and Morse, 2001; Hilgers and Urai, 2005). Based on the presence of (1) diffuse host rock fragment boundaries, (2) CIC microstructures, (3) authigenic albite around WRIs and (4) small solid inclusion particles within the albite grains, the ductile-style deformation of WRIs and vein formation presumably took place in a low-cohesion sediment during early diagenesis. Based on the relative position of lithoclasts on the vein walls and on the average dip angle of the veins, which is roughly equal to the average stratal dip in the BAF-2 well, the observed veins are cemented Mode I type fractures formed with a horizontal orientation. Because the mechanism of vein development (suggested by the microstructures) cannot be reconciled with the morphologies of vein-filling minerals, it can be assumed that the primary texture is not present in the veins. The fact that continuous vein growth results in fibrous crystals suggests that the veins were originally filled with an early fibrous mineral phase that is not present anymore. This hypothetical fibrous phase was replaced at a later stage (preserving the early microstructures) by the observed minerals during diagenetic and hydrothermal processes. According to our conceptual model, compaction, pressure solution, force of crystallisation, elevated pore fluid pressure and seepage forces play roles in the formation of these veins and microstructures. A continuous feedback reaction took place due to increasing overburden load and consolidation, resulting in continuous vein

opening and simultaneous crystallisation along horizontal surfaces. These processes can occur in sediments which have high (but readily degraded) primary effective porosity (e.g. mudrocks and carbonates in which beef veins are the most common) for the formation of actively opening antitaxial veins and therefore for the development of beef veins with CIC structures as well.

## Declaration of competing interest

□ The authors declare that they have no known competing financial interests or personal relationships that could have appeared to influence the work reported in this paper.

## CRediT authorship contribution statement

**Ervin Hrabovszki:** Conceptualization, Writing - original draft.  
**Emese Tóth:** Writing - review & editing. **Tivadar M. Tóth:** Writing - review & editing. **Zoltán Máthé:** Resources, Writing - review & editing. **Félix Schubert:** Supervision, Writing - review & editing.

## Acknowledgements

Access to the BAF-2 core samples was provided by the Public Limited Company for Radioactive Waste Management (RHK Kft.) and the Mecsekérc Ltd. This work was supported by the University of Szeged Open Access Fund [grant number 4571]. András Fall and the anonymous reviewer are thanked for their suggestions and comments that greatly improved the manuscript.

## References

- Ábalos, B., Elorza, J., 2011. Latest Cretaceous cone-in-cone structures and soft-sediment deformation (Basque-Cantabrian Basin, north Spain): a record of deep-marine paleoseismicity? *GSA Bulletin* 123, 427–438. <https://doi.org/10.1130/B30047.1>.
- Árkai, P., Balogh, K., Demény, A., Fórizs, I., Nagy, G., Máthé, Z., 2000. Composition, diagenetic and post-diagenetic alterations of a possible radioactive waste repository site: the Boda Albitic Claystone Formation, southern Hungary. *Acta Geol. Hung.* 43, 351–378.
- Barabás-Stuhl, Á., 1981. A geological study of the microcycles forming the Kővágószőlő Sandstone Formation. *Földtani Kozlony* 111, 26–42 (in Hungarian with English abstract).
- Benkovics, L., Mansy, J.-L., Csontos, L., Beregart, F., 1997. Folding in the abaliget road cut (Mecsek mts). *Acta Geol. Hung.* 40, 425–440.
- Beregart, F., Csontos, L., 1988. Brittle tectonics and paleo-stress field in the Mecsek and Villány Mts (Hungary): correlation with the opening mechanism of the Pannonian Basin. *Acta Geol. Hung.* 31, 81–100.
- Bernáth, Gy., Gärtner, D., Zilahi-Sebess, L., Prohászka, A., Hegedűs, S., 2014. A BAF-2 Jelű Fúrás Mélyfúrás-Geofizikai Dokumentálása és Értékelése. (Geophysical Documentation and Evaluation of the BAF-2 Well). Research Report. In: Bernáth, Gy (Ed.). *Geo-Log Geophysical & Environmental Ltd., Budapest* (in Hungarian).
- Bons, P.D., 2000. The formation of veins and their microstructures. *J. Virtual Explor.* 2 <https://doi.org/10.3809/jvirtex.2000.00007>.
- Bons, P.D., Elburg, M.A., Gomez-Rivas, E., 2012. A review of the formation of tectonic veins and their microstructures. *J. Struct. Geol.* 43, 33–62. <https://doi.org/10.1016/j.jsg.2012.07.005>.
- Cobbold, P.R., Rodrigues, N., 2007. Seepage forces, important factors in the formation of horizontal hydraulic fractures and bedding-parallel fibrous veins ('beef' and 'cone-in-cone'). *Geofluids* 7, 313–322. <https://doi.org/10.1111/j.1468-8123.2007.00183.x>.
- Cobbold, P.R., Zanella, A., Rodrigues, N., Løseth, H., 2013. Bedding-parallel fibrous veins (beef and cone-in-cone): worldwide occurrence and possible significance in terms of fluid overpressure, hydrocarbon generation and mineralization. *Mar. Petrol. Geol.* 43, 1–20. <https://doi.org/10.1016/j.marpetgeo.2013.01.010>.
- Cox, S.F., 1987. Antitaxial crack-seal vein microstructures and their relationship to displacement paths. *J. Struct. Geol.* 9, 779–787. [https://doi.org/10.1016/0191-8141\(87\)90079-4](https://doi.org/10.1016/0191-8141(87)90079-4).
- Csontos, L., Benkovics, L., Beregart, F., Mansy, J.-L., Wórum, G., 2002. Tertiary deformation history from seismic section study and fault analysis in a former European Tethyan margin (the Mecsek-Villány area, SW Hungary). *Tectonophysics* 357, 81–102. [https://doi.org/10.1016/S0040-1951\(02\)00363-3](https://doi.org/10.1016/S0040-1951(02)00363-3).
- Csontos, L., Beregart, F., 1992. Reevaluation of the neogene brittle tectonics of the mecsek-villány area (SW Hungary). *Annales universitatis scientiarum budapestinensis de Rolando eötvös nominatae. Sectio geologica* 29, 3–12.
- Desarnaud, J., Bonn, D., Shahidzadeh, N., 2016. The Pressure induced by salt crystallization in confinement. *Sci. Rep.* 6, 30856. <https://doi.org/10.1038/srep30856>, 2016.



- Dewers, T., Ortoleva, P., 1990. Force of crystallization during the growth of siliceous concretions. *Geology* 18, 204–207. [https://doi.org/10.1130/0091-7613\(1990\)018<0204:focdtg>2.3.co;2](https://doi.org/10.1130/0091-7613(1990)018<0204:focdtg>2.3.co;2).
- Dewhurst, D.N., Aplin, A.C., Sarda, J.-P., Yang, Y., 1998. Compaction-driven evolution of porosity and permeability in natural mudstones: an experimental study. *J. Geophys. Res.: Solid Earth* 103 (B1), 651–661. <https://doi.org/10.1029/97jb02540>.
- Dong, G., Morrison, G., Jaireth, S., 1995. Quartz textures in epithermal veins, Queensland; classification, origin, and implication. *Econ. Geol.* 90, 1841–1856. <https://doi.org/10.2113/gsecongeo.90.6.1841>.
- El Tabakh, M., Schreiber, B.C., Warren, J.K., 1998. Origin of fibrous gypsum in the Newark rift basin, eastern North America. *J. Sediment. Res.* 68, 88–99. <https://doi.org/10.2110/jsr.68.88>.
- Fazekas, V., Vincze, J., 1991. Hydrothermal ore indications in the boreholes of the northern foreground of Villány Mountains. *Földtani Kozlony* 121, 23–56 (in Hungarian with English abstract).
- Fedor, F., Hámos, G., Jobbik, A., Máthé, Z., Somodi, G., Szűcs, I., 2008. Laboratory pressure pulse decay permeability measurement of Boda Claystone, Mecsek Mts., SW Hungary. *Phys. Chem. Earth* 33, S45–S53. <https://doi.org/10.1016/j.pce.2008.10.059>.
- Fodor, L., Csontos, L., Bada, G., Györfi, I., Benkovic, L., 1999. Tertiary tectonic evolution of the Pannonian Basin system and neighbouring orogens: a new synthesis of palaeostress data. In: Durand, B., Jolivet, L., Horváth, F., Séranne, M. (Eds.), *The Mediterranean Basins: Tertiary Extension within the Alpine Orogen*, vol. 156. Geological Society, London, Special Publications, pp. 295–334. <https://doi.org/10.1144/gsl.sp.1999.156.01.15>.
- Fossen, H., 2010. *Structural Geology*. Cambridge University Press, Cambridge.
- Fossen, H., Cavalcante, G.C.G., 2017. Shear zones – a review. *Earth Sci. Rev.* 171, 434–455. <https://doi.org/10.1016/j.earscirev.2017.05.002>.
- Fowler, A.C., Yang, X., 1999. Pressure solution and viscous compaction in sedimentary basins. *J. Geophys. Res.: Solid Earth* 104, 12989–12997. <https://doi.org/10.1029/1998jb900029>.
- Franks, P.C., 1969. Nature, origin, and significance of cone-in-cone structures in the Kiowa formation (early cretaceous), north-central Kansas. *J. Sediment. Res.* 39, 1438–1454. <https://doi.org/10.1306/74d71e51-2b21-11d7-8648000102c1865d>.
- Gale, J.F.W., Laubach, S.E., Olson, J.E., Eichhuble, P., Fall, A., 2014. Natural Fractures in shale: a review and new observations. *AAPG (Am. Assoc. Pet. Geol.) Bull.* 98, 2165–2216. <https://doi.org/10.1306/08121413151>.
- Hámos, G., Áron, J., Kovács, S., Nagymarosy, A., Szederkényi, T., 2013. In: Haas, J. (Ed.), *Geology of Hungary*. Springer Berlin Heidelberg. <https://doi.org/10.1007/978-3-642-21910-8>.
- Hilgers, C., Koehn, D., Bons, P.D., Urai, J.L., 2001. Development of crystal morphology during uniaxial growth in a progressively widening vein: II. Numerical simulations of the evolution of antitaxial fibrous veins. *J. Struct. Geol.* 23, 873–885. [https://doi.org/10.1016/S0191-8141\(00\)00160-7](https://doi.org/10.1016/S0191-8141(00)00160-7).
- Hilgers, C., Pennock, G., Schlöder, Z., Burligam, S., Urai, J.L., 2006. Microstructures of fibrous halite veins. In: Philipp, S., Leiss, B., Vollbrecht, A., Tanner, D., Gudmundsson, A. (Eds.), 11. Symposium "Tektonik, Struktur- und Kristallineologie. Universitätsverlag Göttingen. <https://doi.org/10.17875/gup2006-222>.
- Hilgers, C., Urai, J.L., 2005. On the arrangement of solid inclusions in fibrous veins and the role of the crack-seal mechanism. *J. Struct. Geol.* 27, 481–494. <https://doi.org/10.1016/j.jsg.2004.10.012>.
- Horváth, F., Bada, G., Szafián, P., Tari, G., Ádám, A., Cloetingh, S., 2006. Formation and deformation of the Pannonian Basin: constraints from observational data. In: Gee, D. G., Stephenson, R.A. (Eds.), *European Lithosphere Dynamics* 32, 191–206. Geological Society, London, Memoirs. <https://doi.org/10.1144/gsl.mem.2006.032.01.11>.
- Horváth, F., Musitz, B., Balázs, A., Végh, A., Uhrin, A., Nádor, A., Koroknai, B., Pap, N., Tóth, T., Wörum, G., 2015. Evolution of the Pannonian basin and its geothermal resources. *Geothermics* 53, 328–352. <https://doi.org/10.1016/j.geothermics.2014.07.009>.
- Hrabovszki, E., Tóth, E., Raucsik, B., Varga, A., Schubert, F., 2017. Microstructure and cementation analyses on core samples from the BAF-2 well (Boda Claystone Formation, Mecsek mts). *Földtani Kozlony* 147, 245–264. <https://doi.org/10.23928/foldt.kozl.2017.147.3.245> (in Hungarian with English abstract).
- Hubbert, M.K., Willis, D.G., 1957. Mechanics of hydraulic fracturing. *Trans. Soc. Petrol. Eng. AIME* 210, 153–168.
- Koehn, D., Passchier, C.W., 2000. Shear sense indicators in striped bedding-veins. *J. Struct. Geol.* 22, 1141–1151. [https://doi.org/10.1016/S0191-8141\(00\)00028-6](https://doi.org/10.1016/S0191-8141(00)00028-6).
- Kolokol'tsev, V.G., 2002. The cone-in-cone structure and its origin. *Lithol. Miner. Resour.* 37, 523–535. <https://doi.org/10.1023/A:1020913305000>.
- Konrád, Gy., Halász, A., Sebe, K., Bernáth, Gy., Gärtner, D., Hámos, G., Sámson, M., Máthé, Z., Öbert, V., Benei, B., Magyar, L., 2016. Geological results of the boreholes BAF-1, -1A and -2. In: Dályai, V., Hámos, G. (Eds.), *BCF Research Presentation Day, Pécs* (in Hungarian with English abstract).
- Konrád, Gy., Hámos, G., 2006. Geological aspects of determining high activity radioactive waste depository sites in Hungary and the results of the recent research. *Acta geographica ac geologica et meteorologica Debrecina* 1, 33–38.
- Konrád, Gy., Sebe, K., 2010. New details of young tectonic phenomena in the Western Mecsek Mts and their surroundings. *Földtani Kozlony* 140, 135–162 (in Hungarian with English abstract).
- Konrád, Gy., Sebe, K., Halász, A., Babinszki, E., 2010. Sedimentology of a Permian playa lake: the Boda Claystone Formation, Hungary. *Geologos* 16, 27–41. <https://doi.org/10.2478/v10118-010-0002-1>.
- Land, L.S., Prezbindowski, D.R., 1981. The origin and evolution of saline formation water, Lower Cretaceous carbonates, south-central Texas, U.S.A. *J. Hydrol.* 54, 51–74. [https://doi.org/10.1016/0022-1694\(81\)90152-9](https://doi.org/10.1016/0022-1694(81)90152-9).
- Lash, G.G., Engelder, T., 2005. An analysis of horizontal microcracking during catagenesis: Example from the Catskill delta complex. *AAPG (Am. Assoc. Pet. Geol.) Bull.* 89, 1433–1449. <https://doi.org/10.1306/05250504141>.
- Lenti, F., Azbej, T., Németh, B., Szabó, Cs., 2010. Fluid inclusion study on the barite-calcite veins of the Boda Aleurolite Formation (Mecsek Mts., Hungary). *Acta Mineral. Petrogr. Abstr. Ser.*, Szeged 6, 201.
- Lovering, T.G., 1972. Jasperoid in the United States; its Characteristics, Origin, and Economic Significance. U. S. Geological Survey. <https://doi.org/10.3133/pp710>. Professional Paper 710.
- Maros, Gy., Koroknai, B., Palotás, K., Fodor, L., Dudko, A., Forián-Szabó, M., Zilahi-Sebess, L., Bán-Györi, E., 2004. Tectonic Analysis and Structural Evolution of the North-Eastern Mórág Block. Annual Report of the Geological Institute of Hungary, 2003, pp. 371–386.
- Máthé, Z., 2015. Results of Mineralogical, Petrological and Geochemical Investigation of Boda Claystone Formation. PhD thesis. Eötvös Loránd University (in Hungarian with English summary).
- Máthé, Z., Varga, A., 2012. "Ízesítő" a permiai Boda Agyagkő Formáció öskörnyezeti rekonstrukciójához: kőso utáni pseudomorfozák a BAT-4 fúrás agyagkőmintáiban. ("Flavoring" for the environmental reconstruction of the Permian Boda Claystone Formation: Pseudomorphs after halite crystals in core samples from the BAT-4 well). *Földtani Kozlony* 142, 201–204 (in Hungarian).
- Means, W.D., Li, T., 2001. A laboratory simulation of fibrous veins: some first observations. *J. Struct. Geol.* 23, 857–863. [https://doi.org/10.1016/S0191-8141\(00\)00158-9](https://doi.org/10.1016/S0191-8141(00)00158-9).
- Meng, Q., Hooker, J., Cartwright, J., 2017. Early overpressuring in organic-rich shales during burial: evidence from fibrous calcite veins in the Lower Jurassic Shales-with-Beef Member in the Wessex Basin, UK. *J. Geol. Soc.* 174, 869–882. <https://doi.org/10.1144/jgs2016-146>.
- Meng, Q., Hooker, J., Cartwright, J., 2018a. Displacive Widening of Calcite Veins in Shale: Insights Into the Force of Crystallization. *J. Sediment. Res.* 88, 327–343. <https://doi.org/10.2110/jsr.2018.18>.
- Meng, Q., Hooker, J., Cartwright, J., 2018b. Role of pressure solution in the formation of bedding-parallel calcite veins in an immature shale (Cretaceous, southern UK). *Geol. Mag.* 156, 918–934. <https://doi.org/10.1017/S0016756818000377>.
- Obika, B., Freer-Hewish, R.J., Newill, D., 1992. Physico-chemical aspects of soluble salt damage to thin bituminous road surfacing. In: *Pre-Conference Proceedings of International Conference on the Implications of Ground Chemistry and Microbiology for Construction*, University of Bristol, 29 June to 1 July 1992.
- Passchier, C.W., Trouw, R.A.J., 2005. *Microtectonics*, second ed. Springer Berlin Heidelberg. <https://doi.org/10.1007/3-540-29359-0>.
- Plummer, P.S., Gostin, V.A., 1981. Shrinkage Cracks: Desiccation or Synaeresis? *J. Sediment. Res.* 51, 1147–1156. <https://doi.org/10.1306/2127fe4b-2b24-11d7-8648000102c1865d>.
- Ramsay, J.G., 1980. The crack-seal mechanism of rock deformation. *Nature* 284, 135–139. <https://doi.org/10.1038/284135a0>.
- Ramsay, J.G., Huber, M.L., 1983. *The Techniques of Modern Structural Geology. In: Strain Analysis*, vol. 1. Academic Press, London.
- Renard, F., Andréani, M., Boullier, A.-M., Labaume, P., 2005. Crack-seal patterns: records of uncorrelated stress release variations in crustal rocks. *Geol. Soc. Lond. Special Publ.* 243, 67–79. <https://doi.org/10.1144/gsl.sp.2005.243.01.07>.
- Rodrigues, N., Cobbald, P.R., Loseth, H., Ruffet, G., 2009. Widespread bedding-parallel veins of fibrous calcite ("beef") in a mature source rock (Vaca Muerta Fm, Neuquén Basin, Argentina): evidence for overpressure and horizontal compression. *J. Geol. Soc.* 166, 695–709. <https://doi.org/10.1144/0016-76492008-111>.
- Rutter, E., Mecklenburgh, J., Taylor, K., 2017. Geomechanical and petrophysical properties of mudrocks: introduction. *Geol. Soc. Lond. Special Publ.* 454, 1–13. <https://doi.org/10.1144/sp454.16>.
- Rutter, E.H., 1986. On the nomenclature of mode of failure tension on rocks. *Tectonophysics* 122, 381–387. [https://doi.org/10.1016/0040-1951\(86\)90153-8](https://doi.org/10.1016/0040-1951(86)90153-8).
- Sámson, M. (Ed.), 2015. BAF-2 Fúrás Dokumentáció és Értékelő Jelentése. (Documentation and Evaluation of the BAF-2 Well). Research Report. Public Limited Company for Radioactive Waste Management (RHK Kft.), Pécs (in Hungarian).
- Schmidt, R.A., 1977. Fracture mechanics of oil shale – unconfined fracture toughness, stress corrosion cracking, and tension test results. In: Wang, F.-D., Clark, G.B. (Eds.), *The 18th U.S. Symposium on Rock Mechanics*. Golden, Colorado.
- Sebe, K., 2017. Structural evolution of the Mecsek–Villány area (SW Hungary) during post-rift phase and basin inversion. In: Horvat, M., Wacha, L. (Eds.), 7th International Workshop "Neogene of Central and South-Eastern Europe". Velika, Croatia.
- Selles-Martinez, J., 1994. New insights in the origin of cone-in-cone structures. *Carbonates Evaporites* 9, 172–186. <https://doi.org/10.1007/bf03175229>.
- Shaub, B.M., 1937. The origin of cone-in-cone and its bearing on the origin of concretions and septaria. *American Journal of Science* s5– 34, 331–344. <https://doi.org/10.2475/ajs.s5-34.203.331>.
- Sorby, H.C., 1860. On the origin of "Cone-in-Cone". In: *Report of the British Association for the Advance of Science. 29th Meeting* (1859).
- Taber, S., 1916. The growth of crystals under external pressure. *Am. J. Sci.* s4–41, 532–556. <https://doi.org/10.2475/ajs.s4-41.246.532>.
- Tarr, W.A., 1922. Cone-in-Cone. *American Journal of Science* s5–4 199–213. <https://doi.org/10.2475/ajs.s5-4.21.199>.
- Terzaghi, K., Peck, R.B., Mesri, G., 1996. *Soil Mechanics in Engineering Practice*, third ed. Wiley, New York City.
- Tóth, E., Hrabovszki, E., Steinbach, G., Schubert, F., 2018. Quantitative estimation of shear strain and volume change using sigmoidal tension gashes. *Földtani Kozlony* 148, 367–380. <https://doi.org/10.23928/foldt.kozl.2018.148.4.367>.

- Twiss, R.J., Moores, E.M., 1992. *Structural Geology*. W.H. Freeman and Company, New York.
- Van der Pluijm, B.A., Marshak, S., 2004. *Earth Structure*, second ed. W.W. Norton & Company, New York.
- Varga, A., 2009. *Petrology and Geochemistry of the Paleozoic–Lower Triassic Siliciclastic Rocks from Southern Transdanubia, Hungary*. PhD thesis. Eötvös Loránd University (in Hungarian with English summary).
- Varga, A., Raucsik, B., Szakmány, Gy, Máthé, Z., 2006. Mineralogical, petrological and geochemical characteristics of the siliciclastic rock types of Boda Siltstone Formation. *Foldtani Kozlony* 136, 201–231 (in Hungarian with English abstract).
- Varga, A., Szakmány, Gy, Raucsik, B., Máthé, Z., 2005. Chemical composition, provenance and early diagenetic processes of playa lake deposits from the Boda Siltstone Formation (Upper Permian), SW Hungary. *Acta Geol. Hung.* 48, 49–68. <https://doi.org/10.1556/AGeol.48.2005.1.2>.
- Vernik, L., 2016. *Seismic Petrophysics in Quantitative Interpretation*. Society of Exploration Geophysicists, Tulsa. <https://doi.org/10.1190/1.9781560803256>.
- Weyl, P.K., 1959. Pressure solution and the force of crystallization: a phenomenological theory. *J. Geophys. Res.* 65, 2001–2025. <https://doi.org/10.1029/jz064i011p02001>.
- Wiltschko, D.W., Morse, J.W., 2001. Crystallization pressure versus “crack seal” as the mechanism for banded veins. *Geology* 29, 79–82. [https://doi.org/10.1130/0091-7613\(2001\)029<0079:cpvcsa>2.0.co;2](https://doi.org/10.1130/0091-7613(2001)029<0079:cpvcsa>2.0.co;2).
- Woodland, B.G., 1964. The nature and origin of cone-in-cone structure. *Fieldiana Geol.* (New. Ser.) 13, 185–305. <https://doi.org/10.5962/bhl.title.2709>.
- Yang, X., 2000. Pressure solution in sedimentary basins: effect of temperature gradient. *Earth Planet Sci. Lett.* 176, 233–243. [https://doi.org/10.1016/S0012-821X\(99\)00321-0](https://doi.org/10.1016/S0012-821X(99)00321-0).